

博士學位論文

Search for Neutron-Antineutron Oscillation in Super-Kamiokande

全南大學校 大學院

物 理 學 科

張 智 勝

指導教授 金 在 律

2007年 2月



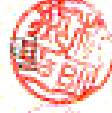


Search for neutron-antineutron oscillation in Super-Kamiokande

全南大學校 大學院

物 理 學 科

張 智 勝

上記者의 理學博士 學位論文을 認准함

| | 所 屬 | 職 位 | 學 位 | 姓 名 |
|---------|----------------|-----|------|---|
| 審查委員長 | 全南大學校 物理教育科 | 敎 授 | 理學博士 | 임 인 복  |
| 審 查 委 員 | 서울大學校 物理學科 | 敎 授 | 理學博士 | 김 수 복  |
| 審 查 委 員 | 東新大學校 物理學科 | 敎 授 | 理學博士 | 박 명 복  |
| 審 查 委 員 | 全南大學校 物理學科 | 敎 授 | 理學博士 | 천 병 규  |
| 審 查 委 員 | 全南大學校 物理學科 | 敎 授 | 理學博士 | 김 재 돌  |

2007年 2月

Contents

| | | |
|----------|--|-----------|
| 1 | Introduction | 1 |
| 2 | Physics of $n - \bar{n}$ Oscillation | 4 |
| 2.1 | Beyond the Standard Model : Grand Unification Theory . . . | 4 |
| 2.1.1 | SU(5) | 4 |
| 2.1.2 | SO(10) | 6 |
| 2.2 | Prediction for $n - \bar{n}$ Oscillation in L-R Symmetric Gauge Theory | 7 |
| 2.3 | Phenomenology of Neutron Oscillations | 8 |
| 2.3.1 | Free Neutron Oscillations | 9 |
| 2.3.2 | Oscillation of Neutrons in an External Field | 10 |
| 3 | Super-Kamiokande | 11 |
| 3.1 | Cherenkov Radiation | 11 |
| 3.2 | Detector | 12 |
| 3.2.1 | Water Tank | 12 |
| 3.2.2 | Photomultiplier Tubes | 13 |
| 3.2.3 | PMT Support Structure and Others | 16 |
| 3.2.4 | Water Purification | 18 |
| 3.2.5 | Electronics and Data Acquisition System | 18 |
| 3.3 | Calibrations | 22 |
| 3.3.1 | Water Transparency Measurement | 22 |
| 3.3.2 | Relative Gain Calibration | 26 |
| 3.3.3 | Relative Timing Calibration | 27 |
| 3.3.4 | Other Calibrations | 27 |
| 4 | Simulation | 29 |
| 4.1 | $n - \bar{n}$ Oscillation | 29 |
| 4.1.1 | Annihilation and Pionization | 31 |
| 4.1.2 | Pion Propagation | 31 |
| 4.1.3 | Fragmentation | 32 |
| 4.2 | Atmospheric Neutrino | 34 |
| 4.2.1 | Neutrino Flux | 34 |
| 4.2.2 | Neutrino Interactions | 38 |
| 4.3 | Detector Simulation | 42 |
| 5 | Data Reduction and Reconstruction: Fully-Contained Events | 45 |
| 5.1 | Data Reduction | 45 |
| 5.1.1 | 1st and 2nd Reduction | 46 |
| 5.1.2 | Third Reduction | 46 |

| | | |
|----------|---|-----------|
| 5.1.3 | Fourth Reduction | 47 |
| 5.1.4 | Fifth Reduction | 47 |
| 5.2 | Reconstruction | 47 |
| 5.2.1 | Vertex Fitting | 48 |
| 5.2.2 | Ring Counting | 48 |
| 5.2.3 | Particle Identification | 49 |
| 5.2.4 | Precise Vertex Fitting and Momentum Determination | 51 |
| 6 | Search for $n - \bar{n}$ Oscillation | 52 |
| 6.1 | Event Selection Criteria | 52 |
| 6.2 | Background | 53 |
| 6.3 | Results | 56 |
| 6.3.1 | Simple Limit Calculation | 57 |
| 6.3.2 | Limit for Free Neutrons | 59 |
| 6.4 | Systematic Errors | 60 |
| 6.4.1 | Uncertainties in Efficiency and Exposure | 60 |
| 6.4.2 | Uncertainties in Background | 63 |
| 6.5 | Final Limit Calculation | 66 |
| 6.5.1 | Description of Method | 66 |
| 6.5.2 | Priors | 67 |
| 6.5.3 | Results | 67 |
| 7 | Conclusion | 68 |

List of Figures

| | | |
|------|---|----|
| 1.1 | Current limits of $n - \bar{n}$ oscillation time. The horizontal axis relates limit for free neutron oscillation time measured in reactor experiment and vertical axis for bound neutron oscillation time in nucleon decay experiments. The bound neutron oscillation time is proportional to the free neutron oscillation time squared with the constant being theoretically determined, nuclear suppression factor. | 3 |
| 2.1 | Running coupling constants g , g' and g_s of the electro-weak and strong interactions appear to extrapolate to a single value at $q \sim 10^{15}$ GeV. | 5 |
| 2.2 | Six quark diagram of $n - \bar{n}$ oscillation. | 8 |
| 3.1 | Cherenkov radiation. | 12 |
| 3.2 | Neutrino event display in the Super-Kamiokande. | 13 |
| 3.3 | Schematic view of Super-Kamiokande. | 14 |
| 3.4 | Schematic view of a 50 cm PMT. | 15 |
| 3.5 | Quantum efficiency of the photocathode as a function of wavelength. | 16 |
| 3.6 | Schematic view of PMT support structure. | 17 |
| 3.7 | Schematic view of water purification system. | 19 |
| 3.8 | A block diagram of ATM board used for inner detector data acquisition. | 20 |
| 3.9 | The data acquisition system for the inner detector. | 20 |
| 3.10 | Outer detector DAQ block diagram and data flow. | 21 |
| 3.11 | Relative photo-sensitivity. (a) Measurement result, (b) Definition of the incident angle. | 22 |
| 3.12 | Effective charge observed as a function of the path length. | 23 |
| 3.13 | Time variation of the water attenuation length measured by through-going. | 23 |
| 3.14 | Laser system for water scattering and absorption parameter measurement and its typical events display. | 24 |
| 3.15 | The upper plot is the photon arrival time distribution of the top PMTs. Dots is data and line is Monte Carlo. The lower plot is the ratio, $(MC-DATA) \times 100 / DATA$ | 25 |
| 3.16 | Time variation measured light attenuation length since November 1999, using the laser system (triangles) and cosmic ray muons (crosses). | 25 |
| 3.17 | The relative gain measurement system. | 26 |
| 3.18 | The timing calibration system. | 28 |

| | | |
|------|---|----|
| 3.19 | A typical plot of timing vs. pulse height. This plot is referred as 'TQ-map'. | 28 |
| 4.1 | Relative position of annihilation in our simulation, labeled as Partnuc. Consistency is checked with Eftrace used in nucleon decay study in Super-K and simulation based on peripheral distribution predicted by Dover is identical to others. | 32 |
| 4.2 | Comparison of interpolated data for pion- ^{16}O cross sections with the predictions of the IMB pion-nucleon interaction model obtained using deuteron scaling. | 33 |
| 4.3 | The absorption probability for pions within 3.5 fermi of the center of the nucleus. Partnuc, the IMB pion interaction program, is based on πd cross section and Eftrace, the Super-K pion interaction program, is based on $\pi^{16}\text{O}$. Our simulation adopts "Scaled O16" which Partnuc was developed with scaled absorption probability. | 33 |
| 4.4 | (a) The direction averaged atmospheric neutrino energy spectrum for $\nu_\mu + \bar{\nu}_\mu$ calculated by several authors are show by solid line[44], dashed line[43] and dotted line[45]. (b) The ratio of the calculated neutrino flux. | 35 |
| 4.5 | The flux ratio of $\nu_\mu + \bar{\nu}_\mu$ to $\nu_e + \bar{\nu}_e$. | 35 |
| 4.6 | The flux ratio of ν_μ to $\bar{\nu}_\mu$ and ν_e to $\bar{\nu}_e$. | 36 |
| 4.7 | The flux of atmospheric neutrinos v. zenith angle. | 37 |
| 4.8 | The flux of upward-going atmospheric neutrinos vs. zenith angle for higher energy region. | 38 |
| 4.9 | Charged current total cross section divided by E_ν for (a) neutrino and (b) anti-neutrino nucleon charged current interactions. Solid line shows the calculated total cross section. The dashed, dot and dash-dotted lines show the calculated quasi-elastic, single-meson and deep-inelastic scattering, respectively. | 41 |
| 4.10 | The cross section of $\pi^{16}\text{O}$ interactions. The lines show the results of our calculation based on [64] and the points show experimental data[66]. | 42 |
| 4.11 | Wavelength dependence of attenuation coefficient (L_{attenu}^{-1}) obtained by light scattering measurement. Point is measurement in Chapter 3.3.1. | 44 |
| 5.1 | The number of hits in the largest outer detector cluster, which is used to separate the fully-contained and partially-contained event samples. The histogram shows the MC prediction with neutrino oscillation. | 46 |
| 5.2 | The distribution of the likelihood difference between a single-ring assumption and a multi-ring assumption for sub-GeV (top) and multi-GeV (bottom) FC events. The hatched histograms show the charged current quasi-elastic interactions. | 49 |
| 5.3 | An event display of a single-ring e -like. | 50 |
| 5.4 | An event display of a single-ring μ -like. | 50 |

| | | |
|-----|--|----|
| 5.5 | The distribution of particle identification likelihood for sub-GeV (top) and multi-GeV (bottom) FC single-ring events, comparing data (points) and atmospheric neutrino MC. The MC includes neutrino oscillation. The hatched histograms show the ν_μ charged current interactions. | 51 |
| 6.1 | Basic plot comparisons : Each plot show Number of rings (Nring), Visible energy (Evis), Total momentum (Ptot) and Total invariant mass (Mtot). Vertical axes are normalized by the number of events and oscillation effect was applied in the case of atmospheric neutrino MC. A peak between 100 and $200MeV/c^2$ of Mtot distribution is caused by π^0 | 54 |
| 6.2 | Visible energy distribution when the number of rings is greater than one. The arrows show the selection region of visible energy for this analysis. | 55 |
| 6.3 | Total momentum and Invariant mass after passing through the selection criterion (a) and (b). | 55 |
| 6.4 | Invariant mass after passing through the selection criterion (a), (b) and (c). | 56 |
| 6.5 | Parent neutrino energy of background events. Left figure shows about 521 background events in total and right figure shows in each interaction mode. | 57 |
| 6.6 | Total invariant mass versus total momentum. The events inside of right lower box in each scatter plot are final sample selected by kinematical cuts for $n - \bar{n}$ oscillation analysis. With 10.4% detection efficiency in which 521 events are detected among 5,000 $n - \bar{n}$ events, 20 candidates and 21 background events are observed. | 58 |
| 6.7 | Fermi momentum distribution. | 61 |
| 6.8 | Likelihood distribution and minimum χ^2 | 63 |
| 6.9 | Likelihood distribution and minimum χ^2 . From the top, it is for 2ring/3more ring separation, 3ring/4more ring separation and 4ring/5more ring separation. | 64 |

List of Tables

| | | |
|-----|---|----|
| 3.1 | Specification of a 50 cm PMT. | 15 |
| 4.1 | $\bar{n} - n$ annihilation branching ratio. | 30 |
| 4.2 | $\bar{n} - p$ annihilation branching ratio. | 30 |
| 4.3 | List of the processes considered in simulator | 43 |
| 5.1 | Number of events after each reduction for fully-contained events during 1489 days of the detector live-time. The Monte Carlo numbers and efficiencies down to the fifth reduction are for events whose real vertex is in the fiducial volume, the number of outer detector hits fewer than 10 and the visible energy larger than 30 MeV. In the last line, the fitted vertex is used for both data and Monte Carlo. | 48 |
| 6.1 | List of background events. | 56 |
| 6.2 | Number of events and detection efficiency after each criterion. | 57 |
| 6.3 | Fitted minimum χ^2 of likelihood function for ring counting. We assume these difference from same reason and change the threshold coherently. | 62 |
| 6.4 | Systematic uncertainties in efficiency and exposure. | 63 |
| 6.5 | Systematic uncertainties in background rate. | 65 |
| 7.1 | The lower limits on $n - \bar{n}$ oscillation time at the 90% <i>CL</i> in nucleon decay experiments. Oscillation time limit is calculated by $T = \epsilon \cdot \lambda/s$. The limits for free neutrons are deduced from the limits for bound neutrons by the suppression factor, $T = R \cdot \tau^2$, and Super-K I limit used a suppression factor of $3.6 \times 10^{23} s^{-1}$ | 69 |

Search for Neutron-Antineutron Oscillation in Super-Kamiokande

Jee-Seung Jang

Department of Physics

Graduate School Chonnam National University

(Directed by Professor Jae-Yool Kim)

(Abstract)

A search for Neutron-Antineutron Oscillation, a process of $|\Delta B| = 2$ predicted by L-R symmetric gauge theories, was undertaken using the 24.5×10^{33} neutron-yr exposure of the Super-Kamiokande I, incorporating most major sources of experimental uncertainties. Observing 20 candidates and 21.6 background events with 10.4 % signal detection efficiency, the lower limit on oscillation time for neutrons bound in ^{16}O has been determined to be 3.20×10^{32} yr at the 90% CL without inclusion of the effect of systematic uncertainties. This limit is better than the previous best limit of 7.2×10^{31} yr in Soudan 2 by a factor of about 4.5. Taking 15.2% uncertainty in efficiency and 32.1% uncertainty in background rate into account, the lower limit for neutrons bound in ^{16}O was estimated to be 1.78×10^{32} yr at the 90% CL and the corresponding limit for free neutrons was calculated to be 1.25×10^8 s using a theoretical suppression factor of $3.6 \times 10^{23} \text{ s}^{-1}$.

Chapter 1

Introduction

The Baryon Asymmetry of the Universe (BAU)[1][2] is one of the most interesting issues in particle physics and particle astrophysics. Baryon instability [3] in combination with CP violation and non-equilibrium thermodynamics in the early Universe, as first suggested by Sakharov, is the most popular explanation of BAU. In the early 1970, attempts at grand unification of the fundamental interactions[4][5] led to the prediction of baryon number as well as lepton number violation and even within the Standard Model it was suggested baryon number was not conserved at the non-perturbative level[6]. Well established theories such as above have encouraged experimentalists to continue the search for baryon instability, even though direct experimental evidence supporting baryon number violation has not been found yet.

In the 1980's, people began to be interested in experimental searches of $n - \bar{n}$ oscillation (a process that was originally referred to neutron transitions) with $|\Delta B| = 2$ rather than usual nucleon decay of $|\Delta B| = 1$. It's interesting to review the motivation behind first experimental search. In 1974, Georgi and Glashow made first predictions regarding observable nucleon decay modes with $|\Delta B| = 1$ such as $p \rightarrow e^+\pi^0$, $p \rightarrow \bar{\nu}K^+$ and $p \rightarrow \mu^+K^0$ which are favored in minimal SU(5) conserving $B - L$, which turn out to be dominant modes in minimal SUSY SU(5). This model yields[7] partial lifetimes τ_p/B for $p \rightarrow e^+\pi^0$ and $p \rightarrow \bar{\nu}K^+$ are less than about 10^{35} yr and 10^{32} yr respectively but strictly suppresses processes with $|\Delta B| = 2$ that violate $B - L$ such as neutron-antineutron transition, the topic of this dissertation. However, these predictions have been ruled out in recent years by experimental results. In particular, the lifetime limit for $p \rightarrow \bar{\nu}K^+$, a dominant mode of minimal SUSY SU(5), has been shown to be 2.3×10^{33} at the 90%CL in published result of Super-Kamiokande[8]. As minimal SUSY SU(5) has been ruled out by stringent limits on $|\Delta B| = 1$ processes, it has become important to study processes that obey different symmetry laws such as neutron-antineutron oscillation which can occur in large class of supersymmetric $SU(2)_L \otimes SU(2)_R \otimes SU(4)_C$ [9] (Left-Right symmetric gauge group).

The $n - \bar{n}$ oscillation has the additional properties. The $n - \bar{n}$ oscillation occurs at energies $\sim 10^5$ GeV[10] compared to the unification scale of SU(5) $\sim 10^{15} - 10^{16}$ GeV in which $p \rightarrow e^+\pi^0$ would be observable with a lifetime of about 10^{34} yr. Thus, if $n - \bar{n}$ oscillation were to be observed experimentally,

new force of nature beyond the standard model would be discovered at the energy scale above 1 TeV and an explanation of the matter-antimatter asymmetry would be put forward. If it were not to be discovered, it would provide new limit on the stability of the neutrons.

There are two major experimental methods for an $n - \bar{n}$ searches: One of them is utilizing free neutrons from reactors or neutron spallation sources such as the ILL at Grenoble[10] and the other method is monitoring neutrons bound inside the nuclei. In this thesis, neutrons bound in oxygen are studied in Super-Kamiokande (Super-K). Figure 1.1[11] is showing the relationship between the oscillation time limits of free neutron and bound neutron. Two methods are related by theoretical "nuclear suppression factor[12][13][14]".

Super-Kamiokande is the world's largest water Cherenkov detector with a net mass 50,000 tons located in Japan for observing neutrinos from various natural sources such as the Sun, the Earth's atmosphere, supernovae and other astrophysical sources as well as neutrinos from artificial sources such as particle beams. Many significant results were published from the first phase of Super-Kamiokande (called Super-K I) including the world's highest limits on partial lifetimes for nucleon decay in minimal SUSY SU(5) under the condition of $|\Delta B| = 1$. $n - \bar{n}$ oscillation, a process of $|\Delta B| = 2$ is studied in this thesis using the 91.7 kton-yr exposure of Super-K I. Even though searches for this process have been made in various nucleon decay experiments including IMB[15], Kamiokande[16], Fréjus[17] and Soudan[18], it has not to be observed yet. The current best limit for the $n - \bar{n}$ oscillation time for bound neutrons is $T_{Iron} \geq 7.2 \times 10^{31}$ by Soudan 2 for iron nuclei. It has been expected that Super-Kamiokande will greatly improve this limit because it has by far the world's best neutron exposure, although the Sudbury Neutrino Observatory[19] (SNO) is also planning on obtaining a competitive limit for bound neutrons.

In this thesis, $n - \bar{n}$ oscillation is studied using neutrons bound in oxygen nuclei corresponding to 24.5×10^{33} neutron-yr of Super-Kamiokande operating from April, 1996 to July, 2001 (the full Super-K I period). Before describing the $n - \bar{n}$ analysis and result, I'll outline the physics of $n - \bar{n}$ search and Super-K detector. MC simulation to estimate detection efficiency of $n - \bar{n}$ oscillation and the number of background and detector simulation are described in Chapter4 and the reduction and reconstruction for Super-K data are described in Chapter5. In Chapter 6, data analysis methods, procedure and result are described. And the final chapter, Chapter7, contains the conclusions and suggestions for further research on this topic.

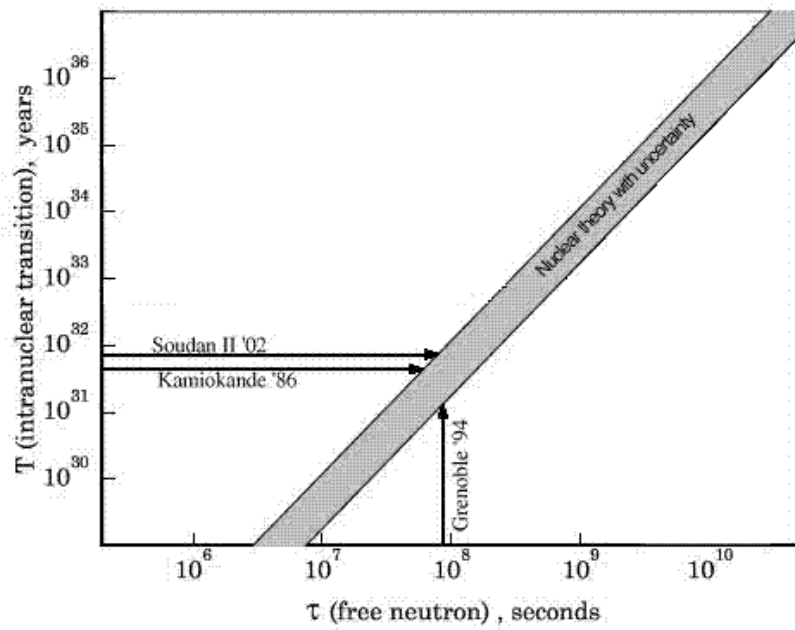


Figure 1.1: Current limits of $n - \bar{n}$ oscillation time. The horizontal axis relates limit for free neutron oscillation time measured in reactor experiment and vertical axis for bound neutron oscillation time in nucleon decay experiments. The bound neutron oscillation time is proportional to the free neutron oscillation time squared with the constant being theoretically determined, nuclear suppression factor.

Chapter 2

Physics of $n - \bar{n}$ Oscillation

$n - \bar{n}$ oscillation was first proposed as a possible explanation of BAU by Kuzmin[2] in 1970 and was developed within the framework of the unification models by Mohapatra etc.[20][21]. In this chapter, theoretical prediction and phenomenology of the $n - \bar{n}$ oscillation are described.

2.1 Beyond the Standard Model : Grand Unification Theory

All known particle physics phenomena are well described within standard model at the low energies. The standard model is a quantum field theory based on the gauge symmetry $SU(3)_C \times SU(2)_L \times U(1)_Y$ which includes the symmetry group of the strong interactions, $SU(3)_C$, and the symmetry group of the electroweak interactions, $SU(2)_L \times U(1)_Y$. In spite of the impressive successes of the standard model, it is a very unsatisfactory model since it leaves many questions unanswered. For examples, there should be only one gauge coupling which implies that all interactions should results from one non-abelian local symmetry. However, standard model has three different group with three different gauge coupling. And Right-handed neutrinos are missed and neutrino masses are assumed to be zero. Moreover this model can not explain Higgs mass and does not include Gravity.

In this section, physics beyond the standard model is described with Grand Unification Theory (GUT). The most interesting GUT groups are $SU(5)$, $SO(10)$ and E_6 . Since all these groups unify baryon and leptons, they lead to baryon violating processes such as proton decay, $p \rightarrow e^+ \pi^0$ and $n - \bar{n}$ oscillation. Different models predict different strengths for these baryon violating processes and experimental information on these processes will provide tests of various GUT models. In order to have observable $n - \bar{n}$ oscillation one needs a low scale (~ 100 TeV) unification symmetry group $SU(2)_L \otimes SU(2)_R \otimes SU(4)_C$ which is one intermediate stage to break $SO(10)$ symmetry.

2.1.1 SU(5)

With the success of the unified theory of electro-weak interactions in SM, it became natural to ask whether the strong interaction could also be united

with the weak and electromagnetic interactions into a single. The basic idea of the approach to a universal coupling is illustrated in Figure 2.1.

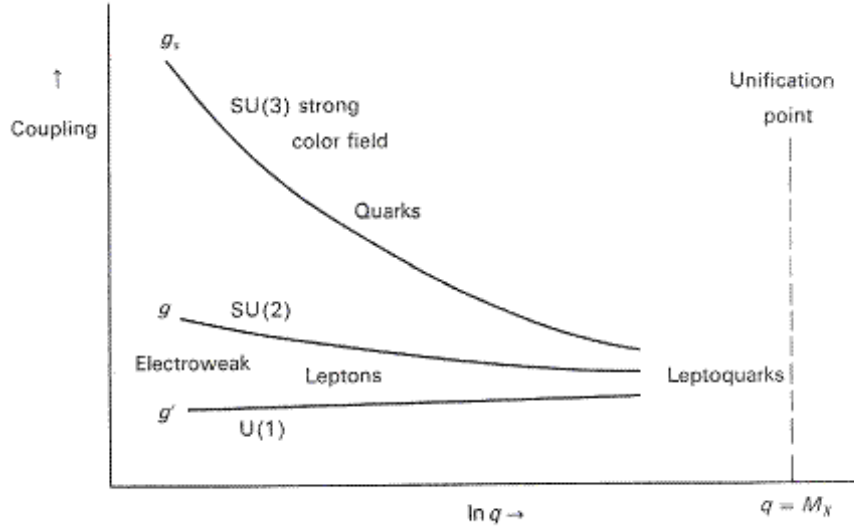


Figure 2.1: Running coupling constants g , g' and g_s of the electro-weak and strong interactions appear to extrapolate to a single value at $q \sim 10^{15}$ GeV.

The graph indicates the dependence on momentum transfer, or mass scale, of the running coupling constants for the Abelian $U(1)$ field described by g' , for the non-Abelian $SU(2)$ field denoted by g , and for the non-Abelian $SU(3)$ color field which we denote g_s (where $\alpha_s = g_s^2/4\pi$). As q increases, g' increases slightly while g decreased slightly and g_s decreased more quickly. It is a remarkable fact that when all three interactions are extrapolated, they appear to meet at a single point at the colossal value of $q \simeq 10^{15}$ GeV. (There are numerical constants of order unity multiplying g , g' and g_s , which we have omitted from Figure 2.1. Implicit in this enormous extrapolation is the bold assumption that Nature has run out of ideas and has no new surprises in the range from $q \simeq 30$ GeV/c of present accelerator experiments, all the way to $q \simeq 10^{15}$ GeV/c. There may instead be new internal degrees of freedom, quark or lepton substructure, only just around the corner and to be revealed at the next generation of accelerators. On the basis of past experience, one would think that this is rather likely.

There are many ways in which the $SU(2)$, $U(1)$ and $SU(3)$ symmetries could be incorporated into a more global gauge symmetry. The simplest grand unifying symmetry is that of the group $SU(5)$ -Georgi and Glashow, 1974. This incorporates the known fermions (leptons and quarks) in multiplets, inside which quarks can transform to leptons, and quarks to anti-quarks, via the mediation of very massive (10^{15} GeV) bosons Y and X , with electric charges $-1/3$ and $-4/3$ respectively. There are a total of 24 gauge bosons in the model. These consist of the 8 gluons of $SU(3)$ and the W^\pm , Z^0 and photon of $SU(2) \times U(1)$, plus the 12 varieties of X and Y boson (each carrying 3 colors and existing in particle and antiparticle states). The fermions (quarks and leptons) are assigned to different "generations", The first gener-

ation consists of 15 states: the u- and d-quarks, each in 3 color and 2 helicity states; the e^- with 2 helicity states; and the ν_e , with 1 helicity only. By convention, we write them down as LH states, since, for example, the e^-_{RH} state and the e^+_{LH} state are equivalent (by CP). The 15 states comprise "5" and "10" representations as follows:

$$\bar{5} = \begin{pmatrix} \nu_e \\ e^- \\ \bar{d}_R \\ \bar{d}_B \\ \bar{d}_G \end{pmatrix}_{LH} \quad \left. \begin{array}{l} \} \\ \} \\ \} \end{array} \right\} \begin{array}{l} W^- \\ X \\ G_{BG} \end{array} \quad (2.1)$$

The arrows indicate a gluon mediating the color force between quarks, the W^\pm mediating the charged weak current, and an X "leptoquark" boson transforming a quark to a lepton. The quantum numbers of the "10" are obtained from the antisymmetric combinations $q_i q_j - q_j q_i$ of the members q_i of the "5" (conjugates of the \bar{q}_i of the "5"). Thus,

$$10 = \begin{pmatrix} 0 & e^+ & d_R & d_B & d_G \\ -e^+ & 0 & u_R & u_B & u_G \\ -d_R & -u_R & 0 & \bar{u}_G & \bar{u}_B \\ -d_B & -u_B & -\bar{u}_G & 0 & \bar{u}_R \\ -d_G & -u_G & -\bar{u}_B & -\bar{u}_R & 0 \end{pmatrix}_{LH} \quad (2.2)$$

These multiplets have the property that the total electric charge $\Sigma Q_i = 0$. The heavier leptons ($\mu, \nu_\mu, \tau, \nu_\tau$) and quarks (s, c, b) have to be assigned to separate quark-lepton generations.

This model make many predictions, some of which are accessible in present or future experiments. One of them is proton must decay. The favored decay mode is $p \rightarrow e^+ \pi^0$ based on $SU(5)$ symmetry ("minimal $SU(5)$ "). This predicts partial lifetime of $p \rightarrow e^+ \pi^0$ should be less than 1.4×10^{32} yr assuming[22] $\Lambda_{\bar{M}S}$ to be less than 400 MeV. However, first generation nucleon decay experiments, KAMIOKANDE[23] and Irvine-Michigan-Brookhaven[24] (IMB), motivated by this prediction, observed no evidence and ruled out this model. And it turns out that this contradiction to $SU(5)$ can be solved by incorporating supersymmetry (SUSY). This model[7] shows the constance with experimental non-observation of $p \rightarrow e^+ \pi^0$. However, Super-Kamiokande made this model incompatible by non-observation of other dominant mode, $p \rightarrow \bar{\nu} K^+$ over the predicted limit. As the minimal SUSY $SU(5)$ also was ruled out, other extended models are noticed.

2.1.2 SO(10)

The $SO(10)$ symmetry is one of most interesting model to extend the $SU(5)$ GUT since $SO(10)$ has several remarkable advantages.

The $SO(10)$ GUT model which directly breaks to $SU(3)_C \otimes SU(2)_L \otimes U(1)_Y$ predicts relatively short lifetime of protons and the prediction is not consistent with experimental result[25]. On the other hand, there are several ways for $SO(10)$ symmetry to break down to $SU(3)_C \otimes SU(2)_L \otimes U(1)_Y$ by

two steps[26].

$$SO(10) \rightarrow \left(\begin{array}{l} SU(5) \otimes U(1) \\ SU(4) \otimes SU(2)_L \otimes SU(2)_R \\ SU(3) \otimes SU(2)_L \otimes SU(2)_R \otimes U(1) \\ SU(3) \otimes SU(2)_L \otimes U(1) \otimes U(1) \end{array} \right) \rightarrow SU(3)_C \otimes SU(2)_L \otimes U(1)_Y \quad (2.3)$$

One of advantages of $SO(10)$ GUT models is that it can contain the left-right symmetry which is missed in the standard electroweak model. Second advantage is that $SO(10)$ model has representations of 16 in which there is a room for right handed neutrinos(ν_R) missed in the $SU(5)$ model. $SO(10)$ model that implements the seesaw mechanism[27] may explain the neutrino masses and mixing. Moreover, the fermion unification into a single representation of 16 is a attractive feature of the model.

$SO(10)$ models predict $\sin^2\theta_W$ consistent with experimental results and the running coupling constants can meet at a single unification point[28][29]. Among several intermediate symmetries, $SU(4) \otimes SU(2)_L \otimes SU(2)_R$ which was suggested by Pati and Salam[4] in 1973 is very interesting because it contains the left-right symmetry. Within this framework, an immediate implication of $(B-L)$ -symmetry breaking is the existence not only of Majorana neutrinos ($\Delta L = 2$ in the lepton section) but also the new phenomenon of $n \rightarrow \bar{n}$ transition ($\Delta B = 2$ in the hadron sector), which we call "neutron oscillations" [20].

2.2 Prediction for $n - \bar{n}$ Oscillation in L-R Symmetric Gauge Theory

There are many models for $n - \bar{n}$ oscillation. Among them, $SU(2)_L \times SU(2)_R \times SU(4)_C$ which $SU(4)$ unifies color and $B-L$ symmetry is adopted in this section. Following prediction for $n - \bar{n}$ oscillation within this framework is from Mohapatra[10].

Lifetime of $n - \bar{n}$ oscillation for free neutrons is led with observable strength depends on the details of the theory such as value of mass scales etc.

$$\tau_{n-\bar{n}} = \frac{h}{2\pi\delta m_{n-\bar{n}}} \quad (2.4)$$

where h is Plank's constant and $\delta m_{n-\bar{n}}$ is the transition mass for $n \rightarrow \bar{n}$ transition. Within the framework of "partial unification" group $SU(2)_L \times SU(2)_R \times SU(4)_C$ for electroweak and strong interactions, in order to obtain $n - \bar{n}$ oscillation process, the gauge symmetry breaking of the model has to be broken by the Higgs multiplets as in Ref.[21]: A bidoublet, $\phi(2,2,1)$, and a pair of triplets, $\Delta_L(3, 1, \bar{10}) + \Delta_R(1, 3, \bar{10})$. The quarks and leptons are assigned to representations as follows: $Q_L(2, 1, 4) + Q_R(1, 2, 4)$. Here leptons are considered as the fourth color. The allowed Yukawa couplings in the model are given by:

$$L_Y = y_q \bar{Q}_L \phi Q_R + f(Q_L Q_L \Delta_L + Q_R Q_R \Delta_R) + h.c. \quad (2.5)$$

Here all generation indices was omitted and the couplings symbolically omitting charge conjugation matrices, Pauli matrices etc was denoted. The Higgs

potential of the model can be easily written down; the term in it which is interesting for the purpose of this study is $\lambda \varepsilon^{ijkl} \varepsilon^{i'j'k'l'} \Delta_{L,ii'} \Delta_{L,jj'} \Delta_{L,kk'} \Delta_{L,ll'} + L \rightarrow R + h.c..$

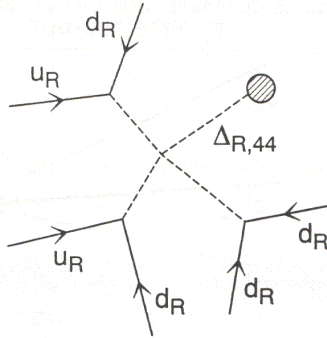


Figure 2.2: Six quark diagram of $n - \bar{n}$ oscillation.

In order to proceed towards the goal of estimating the strength of $n - \bar{n}$ oscillation in this model, we can first note that the original gauge symmetry here is broken by the $\langle \Delta_{R,44} \rangle = v_{B-L} \neq 0$ to the standard model gauge group. The diagram of Figure 2.2[10] then leads to six quark effective interaction below the scale v_{B-L} of the form $u_R d_R d_R u_R d_R d_R$. A rough estimate of the strength of neutron oscillations as follows:

$$A_{n-\bar{n}} \simeq \frac{\lambda f^3 \langle \Delta_R \rangle}{m_{\Delta_R}^6} \quad (2.6)$$

where λ is the scalar self-coupling of the Higgs boson Δ_R , f is the strength of fermion-Yukawa coupling, and m_{Δ_R} is the mass of the Higgs boson Δ_R . For the scale $\langle \Delta_R \rangle$ and m_{Δ_R} of order 100 TeV and for $h \approx \lambda \approx 10^{-1}$ this will lead to a strength for the six quark amplitude of about $10^{-29} \text{ GeV}^{-5}$. In order to convert it to $\delta m_{n-\bar{n}}$, we need the three quark "wave function" of the neutron at the origin. This has been estimated by various people[30] and usually yields a factor of about 10^{-4} or so. With these values, we obtain a lifetime for free neutron oscillations in this model, $\tau_{n-\bar{n}} \simeq 6 \times 10^8$ sec from Eq. (2.4) where $h/2\pi = 6.58 \times 10^{-22} \text{ MeV}\cdot\text{s}$. This oscillation time is related with the nuclear instability life time (This is however only an order of magnitude estimate since the true value of the parameters that go into this estimate is unknown. But the main point that this example makes is that there exist very reasonable theories where $n - \bar{n}$ oscillation is observable. Note that this model is a completely realistic extension of the standard model with many interesting features such as the smallness of neutrino mass naturally explained etc.

2.3 Phenomenology of Neutron Oscillations

This section describes the basic phenomenology of neutron oscillations. First we consider free neutron oscillations and the effect of an external field

on neutron oscillations is treated. In particular the effect of an external magnetic field on the opposite magnetic momentum of n and \bar{n} . This description is by R. N. Mohapatra and R. E. Marshak[31]

2.3.1 Free Neutron Oscillations

The starting point is the $n - \bar{n}$ mass matrix.

$$L_{mass} = \bar{\psi} M \psi \quad (2.7)$$

where

$$\psi = \begin{pmatrix} n \\ \bar{n} \end{pmatrix}$$

and

$$M = \begin{pmatrix} A & \delta m \\ \delta m & A \end{pmatrix} \quad (2.8)$$

In Eq. (1.8), δm is the $\Delta B = 2$ transition mass between n and \bar{n} states. The equality of the diagonal elements follows from CPT invariance and that of the off-diagonal elements from CP invariance. The eigenstates of M can be written as:

$$n_{1,2} = \frac{n \pm \bar{n}}{\sqrt{2}} \quad (2.9)$$

with masses:

$$m_{1,2} = A \pm \delta m \quad (2.10)$$

Next, the amplitude for finding an \bar{n} at time t starting with a beam of neutrons at $t=0$ is:

$$|n(t)\rangle = e^{-\frac{\gamma t}{2}} \left(\frac{|n_1(0)\rangle e^{-im_1 t} + |n_2(0)\rangle e^{-im_2 t}}{\sqrt{2}} \right) \quad (2.11)$$

where we have assumed that the decay widths of n_1 and n_2 are equal and denoted by γ . The probability for finding an \bar{n} at time t , $P_{\bar{n}}(t)$ is:

$$P_{\bar{n}}(t) = \frac{e^{-\gamma t}}{2} (1 - \cos 2\delta m t) \quad (2.12)$$

If $t \ll 1/\gamma m$, then we obtain:

$$P_{\bar{n}}(t) \simeq e^{-\gamma t} (\delta m t)^2 \quad (2.13)$$

The upper limit on δm can be estimated from the upper limit on the $\Delta B = 2$ "bound" nucleon transition rate, $\Gamma_{\Delta B=2}$ by means of the relation:

$$\delta m \simeq \sqrt{\Gamma_{\Delta B=2} M} \quad (2.14)$$

Here, M is a typical hadronic mass. This part will be explained again in Chapter 6.3.2. Anyway, it follows that if a beam of N free neutrons is allowed to travel for a time T before hitting a target, the number of antineutrons, \bar{N} , at the target after T should be (assuming $\gamma T \ll 1$):

$$\bar{N} \leq N \left(\frac{T}{\tau_{n-\bar{n}}} \right)^2 \quad (2.15)$$

$\tau_{n-\bar{n}}$ is $n - \bar{n}$ oscillation time. With reasonable values of N and T , above equation would be rather promising for a "free" neutron oscillation experiment. However, there is a complicating factor resulting from the presence of the earth's magnetic field which shifts the energy of n and \bar{n} by opposite amounts $\pm\mu B \sim 10^{-11}$ eV, which is much larger than δm . We deal with this situation in the next section.

2.3.2 Oscillation of Neutrons in an External Field

If the neutron oscillation takes place in an external field (such as the earth's magnetic field or other field) so that the CPT theorem need not be respected, the picture outlined in previous section changes and we have:

$$M = \begin{pmatrix} A1 & \delta m \\ \delta m & A2 \end{pmatrix} \quad (2.16)$$

The neutron mass eigenstates in this case are:

$$\begin{aligned} |n_1\rangle &\simeq |n\rangle + \theta|\bar{n}\rangle \\ |n_2\rangle &\simeq -\theta|n\rangle + |\bar{n}\rangle \end{aligned}$$

where

$$\theta \simeq \delta m / \Delta M \quad (2.17)$$

where $\Delta M \equiv M_1 - M_2 \approx A_1 - A_2 \gg \delta m$. And probability is:

$$P_{\bar{n}}(t) \simeq \frac{\theta^2}{2} [1 - \cos \Delta M t] \quad (2.18)$$

Above equation is interesting in two limiting cases: (a) $\Delta M t \gg 1$ and (b) $\Delta M t \ll 1$. In case (a), the second term oscillates rapidly and the average probability for finding an \bar{n} , $\langle P_{\bar{n}} \rangle_{av}$ becomes:

$$\langle P_{\bar{n}} \rangle_{av} \simeq \left(\frac{\delta m}{\Delta M} \right)^2 \quad (2.19)$$

In case (b), we get:

$$P_{\bar{n}}(t) \simeq (\delta m t)^2 \quad (2.20)$$

as long as $\gamma t \ll 1$.

Chapter 3

Super-Kamiokande

Super-Kamiokande is the world's largest water Cherenkov detector with a net mass 50,000 tons located in Muzumi mine, Gifu, Japan. Detector cavity lies under the peak of Mt. Ikenoyama with 1,000 meters of rock or 2,700 meter-water-equivalent mean overburden. The scientific goal of this experiment is observing neutrinos from various natural sources such as the Sun, the Earth's atmosphere, supernovae and other astrophysical sources as well as neutrinos from artificial sources such as particle beams and includes nucleon decay search. Super-Kamiokande began to take data in April, 1996. This operating was shut down for maintenance and upgrade in July, 2001. This running period is referred to as Super-Kamiokande I (Super-K I). During refilling the water to start Super-Kamiokande II, in November, 2001, an apparent cascade of implosions triggered by a single photomultiplier tube (PMT) implosion destroyed over half of the PMTs installed in the detector. In 2002, the detector was reconstructed with 5,000 PMTs (the original number of PMTs used in Super-K is 11,146) encased in acrylic covers to avoid a similar accident. After partial reconstruction, Super-Kamiokande II was operated from Dec. 2002 to Oct. 2005 with temporarily reduced PMT coverage (47% of Super-K I). In June 2006, the third phase experiment, Super-Kamiokande III, has been started after full reconstruction recovering PMT coverage as Super-K I. In this thesis, 4.07 years data in Super-K I period is used for analysis. The configuration and operational characteristics of the detector in the Super-K I period are described in this chapter based on [32].

3.1 Cherenkov Radiation

The Super-Kamiokande is water Cherenkov detector which observed relativistic charged particles in water by detecting the Cherenkov light. Cherenkov photons are radiated when a charged particle in a material medium moves faster than the speed of light in that same medium. Therefore a particle emitting Cherenkov radiation must have a velocity

$$v_{particle} \geq \frac{c}{n} \quad (3.1)$$

where n is the index of refraction and c is the speed of light in a vacuum[33]. The momentum threshold of Cherenkov radiation is determined by the re-

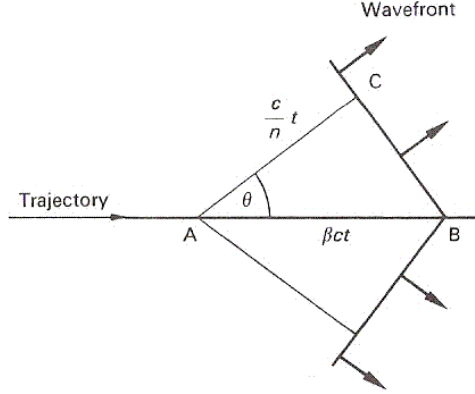


Figure 3.1: Cherenkov radiation.

refractive index of the medium and the mass of particle. In water, the refractive index is about 1.34, and the momentum threshold for electrons, muons and pions are 0.57, 118 and 156 MeV/c, respectively.

This radiation creates electromagnetic shock wave. This is illustrated in Figure 3.1. The coherent wave front formed is conical in shape and is emitted at a well-defined angle

$$\cos\theta_C = \frac{1}{n\beta} \quad (3.2)$$

with respect to the trajectory of the particle where $\beta = v/c$ and this angle is called as Cherenkov angle. For the particle with $\beta \simeq 1$ in water, the Cherenkov angle is about 42° . This angle is dependent on the speed of the particles and the frequency of the emitted radiation.

The number of photons emitted by Cherenkov radiation is given as a function of the wave length λ as follows;

$$\frac{d^2 N}{dx d\lambda} = \frac{2\pi\alpha}{\lambda^2} \left(1 - \frac{1}{n^2\beta^2}\right) \quad (3.3)$$

where x is the path length of the charged particle and α is the fine structure constant. About 340 photons/cm are emitted between the wavelength of 300nm to 600nm, which is the sensitive wavelength region of photomultiplier tubes. Particle emitting Cherenkov light projects ring images on the wall inside of the detector. Figure 3.2 shows display of a typical neutrino event in the Super-Kamiokande detector.

3.2 Detector

3.2.1 Water Tank

Figure 3.3 shows the schematic view of detector. The outer shell of the detector is a cylindrical stainless steel tank, 39 m in diameter and 42m in height. The tank is self-supporting, with concrete backfilled against the

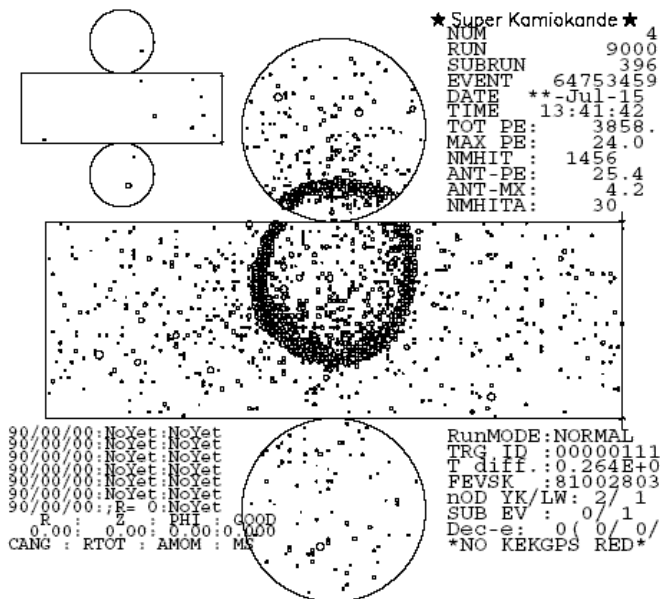


Figure 3.2: Neutrino event display in the Super-Kamiokande.

rough-hewn stone walls to counteract water pressure when the tank is filled with water. The capacity of the tank exceeds 50 ktons of water. A cylindrical PMT support structure divides the tank into two distinct, optically isolated volumes. The structure has inner dimensions, 33.8 m (diameter) by 36.2 m (height), defining the inner detector (ID) which contains 32 ktons of water and was viewed by inward-facing 50 cm (20 inch) PMTs (Hamamatsu R3600). Approximately 2.5 m distance remains on all outside of the support structure. This outside region defining outer detector (OD), serves as an active veto counter against incoming particles as well as a passive shield for neutrons and gamma rays from the surrounding rocks. OD was instrumented with 1,885 outward-facing 20 cm (8 inch) PMTs (Hamamatsu R1408). The two detector volumes are isolated from each other by two light-proof sheets on both surfaces of the PMT support structure. The 55 cm thick support structure comprises dead space from which light in principle cannot escape. Therefore, any interaction in that space cannot be detected. The OD PMTs were mounted in water-proof housings which effectively block light from the dead space. However, because the ID PMTs were not fully covered in back, some light generated in this region was still detected by the ID PMTs.

3.2.2 Photomultiplier Tubes

Inner Detector Photomultiplier Tubes

A 50 cm ID PMTs used in this experiment is described in Figure 3.4 and the specifications are summarized in Table 3.1. The bialkali (Sb-K-Cs) photocathode has peak quantum efficiency of about 21% at 360 nm-400 nm as shown in Figure 3.5. The collection efficiency for photoelectrons (pe) at the first dynode is over 70%. The transit time spread for a 1 pe signal is

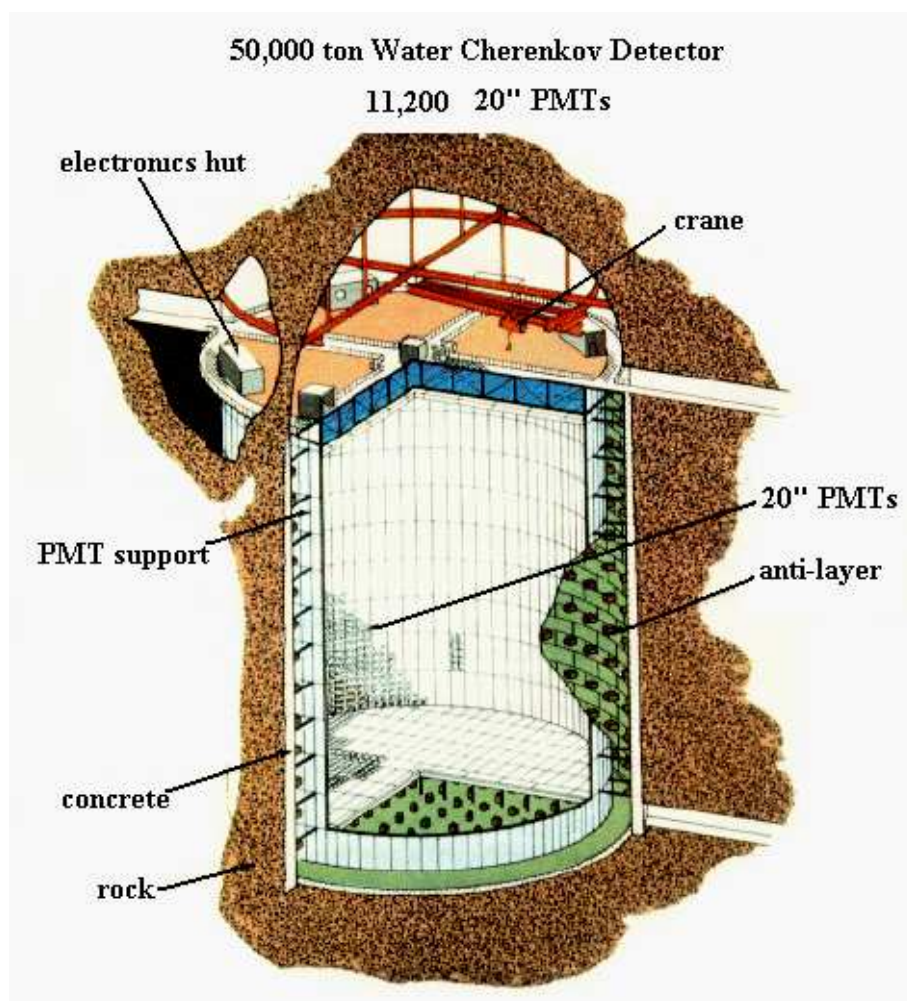


Figure 3.3: Schematic view of Super-Kamiokande.

2.2 ns. The average dark noise rate at the 0.25 pe threshold is about 3 kHz in Super-Kamiokande I. The ID PMTs were operated with gain of 107 at a supply high voltage ranging from 1700 to 2000 V. The neck of each PMT was coated with a silver reflector to block external light.

Outer Detector Photomultiplier Tubes

These PMTs were first adopted in the IMB experiment[34] and they are reused in the Super-Kamiokande after finishing that experiment. Light collection efficiency in the OD PMTs is enhanced by wavelength shifting (WS) plates attached to each OD PMT. The WS plates are square acrylic panels, 60 cm on a side and 1.3 cm thick, doped with 50 mg/l of bis-MSB. The WS plates function by absorbing UV light, and then re-radiating photons in the blue-green, better matching the spectral sensitivity of the PMT's bialkali photocathode. The light collection of the PMT plus WS unit is improved over that of the bare PMT by about a factor of 1.5.

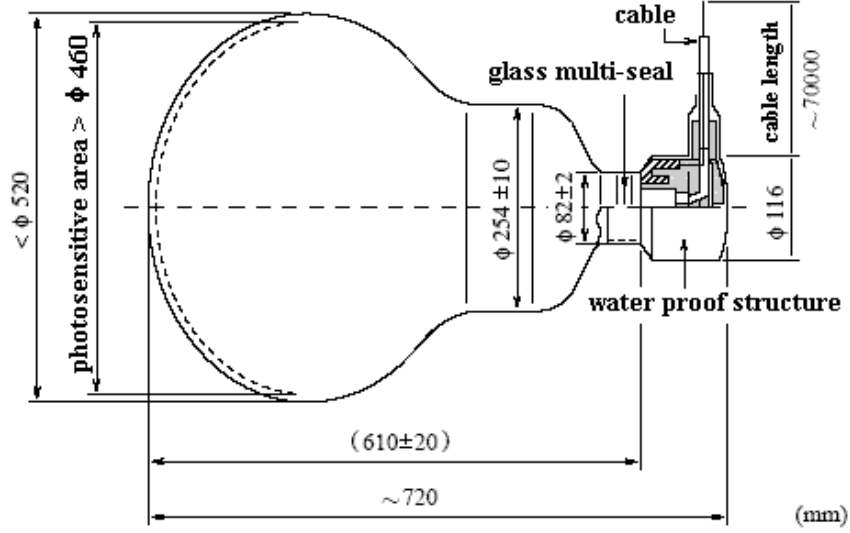


Figure 3.4: Schematic view of a 50 cm PMT.

| | |
|------------------------|---|
| Shape | Hemispherical |
| Photocathode area | 50 cm diameter |
| Window material | Pyrex glass (4 ~ 5 mm) |
| Photocathode material | Bi-alkali (Sb-K-Cs) |
| Quantum efficiency | 22% at $\lambda=390$ nm |
| Dynodes | 11 stage Venetian blind type |
| Gain | 10^7 at ~ 2000 V |
| Dark current | 200 nA at 10^7 gain |
| Dark pulse rate | 3kHz at 10^7 gain |
| Cathode non-uniformity | < 10 % |
| Anodes non-uniformity | < 40 % |
| Transit time | 90 nsec at 10^7 gain |
| Transit time spread | 2.2 nsec (1σ) for 1 p.e. equivalent signals |
| Weight | 13 kg |
| Pressure tolerance | 6 kg/cm ² water proof |

Table 3.1: Specification of a 50 cm PMT.

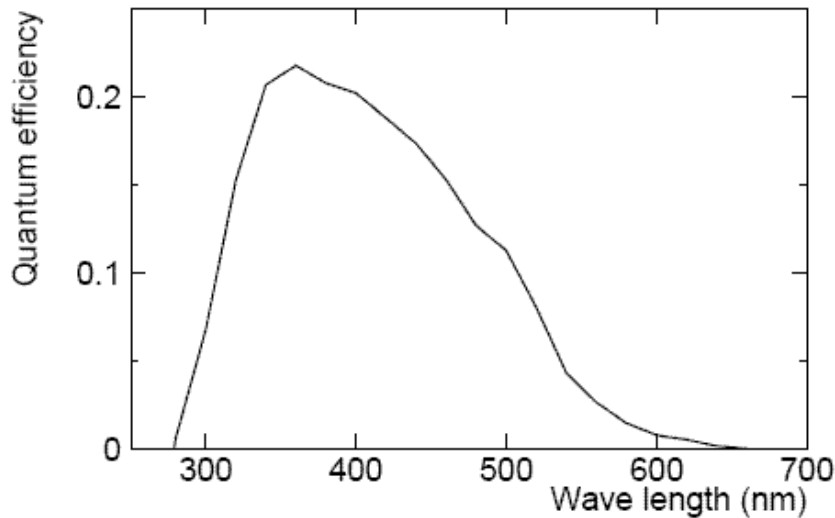


Figure 3.5: Quantum efficiency of the photocathode as a function of wavelength.

3.2.3 PMT Support Structure and Others

Figure 3.6 shows a detail of the PMT support structure. All support structure components are stainless steel. The basic unit for the ID PMTs is a supermodule, a frame which supports a 3x4 array of PMTs. Each supermodule has two OD PMTs attached on its back side. Opaque black polyethylene telephthalate sheets cover the gaps among the PMTs in the ID surface. These sheets improve the optical separation between the ID and OD and suppress unwanted low-energy events due to residual radioactivity occurring behind the PMTs.

Light collection efficiency is enhanced by WS as mentioned in previous section. To further enhance light collection, the OD volume is lined with a reflective layer made from Type 1073B Tyvek manufactured by DuPont. This inexpensive and very tough paper-like material has excellent reflectivity in the wavelength range in which PMTs are most sensitive, especially at short wavelengths. Measured reflectivities are on the order of 90% for wavelengths in excess of 400 nm, falling to 80% at about 340 nm[35]. The presence of this liner allows multiple reflections of Cherenkov light, which minimizes the effects of dead PMTs, given their coarse spacing in the OD. Cherenkov light is spread over many PMTs, reducing pattern resolution but increasing overall detection efficiency.

To protect against low energy background from radon decay products in the air, the roof of the cavity and the access tunnels were sealed with a coating called Mineguard produced by Urylon in Canada. In addition, double doors in the access tunnels restrict air flow from the mine into the detector cavern and "radon-free" air is supplied and radon-reduced air is also produced in the mine.

The average geomagnetic field is about 450 mG and is inclined by about

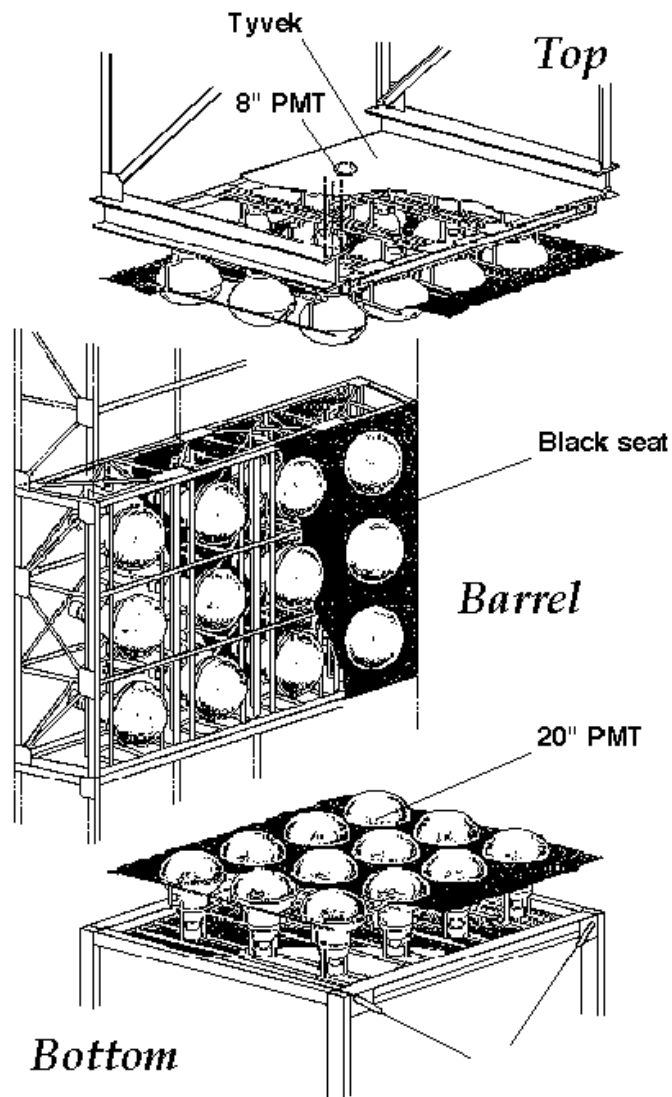


Figure 3.6: Schematic view of PMT support structure.

45° with respect to the horizon at the detector site. The strength and uniform direction of the geomagnetic field could systematically bias photoelectron trajectories and timing in the PMTs. To counteract this, 26 sets of horizontal and vertical Helmholtz coils are arranged around the inner surfaces of the tank. With operation of these coils, the average field in the detector is reduced to about 50 mG. The magnetic field at various PMT locations were measured before the tank was filled with water.

3.2.4 Water Purification

Super-Kamiokande should keep the water transparency as high as possible removing small dust, metal ions like Fe, Ni, Co and bacteria in the water. And radioactive material, mainly Rn, Ra and Th, can be source of background. Especially, radon is serious background for the solar neutrino analysis. However, since there is ~ 60 cm space between the surface of the water and the top of the water tank, radon gas contaminated in the air in the gap could dissolve in the water. Therefore, the 50 ktons of purified water in the Super-Kamiokande tank is continuously reprocessed at the rate of about 30 tons/hour in this closed cycle system. In the Kamioka mine, there is clean water flowing near the detector and it can be used freely in large quantities. This water is circulated through the water purification system shown in Figure 3.7. The water purification system consists of the following components;

- 1 μ m Filter
- Heat exchanger : The water temperature rises due to the heat generated by pumps and PMTs. The temperature is kept at around 14°C to suppress bacteria growth.
- Ion exchanger : This removes metal ions in the water.
- Ultra-Violet sterilize : This kills bacteria. The documentation states the number of bacteria can be reduced to less than $10^3 \sim 10^4/100ml$.
- Vacuum degasifier : This removes gas resolved in the water. It is able to remove about 99% of the oxygen gas and 96% of the radon gas.
- Cartridge polisher : This is a high performance ion exchanger.
- Ultra filter : This remove small dust even of the order of nanometers.

The typical number of particles larger than 0.2 μ m is reduced to 6 particle/cc after purification.

3.2.5 Electronics and Data Acquisition System

Inner Detector Electronics and Data Acquisition

ID PMT signals are processed by custom built TKO modules called Analog-Timing-Modules (ATMs). The TKO (TRISTAN KEK Online) system was originally developed and built by KEK, and is optimized for front-end electronics where a large number of channels are to be handled. The ATM has the functionality of a combined ADC (Analog-to-Digital Converter) and TDC (Time-to-Digital Converter), and records the integrated charge and

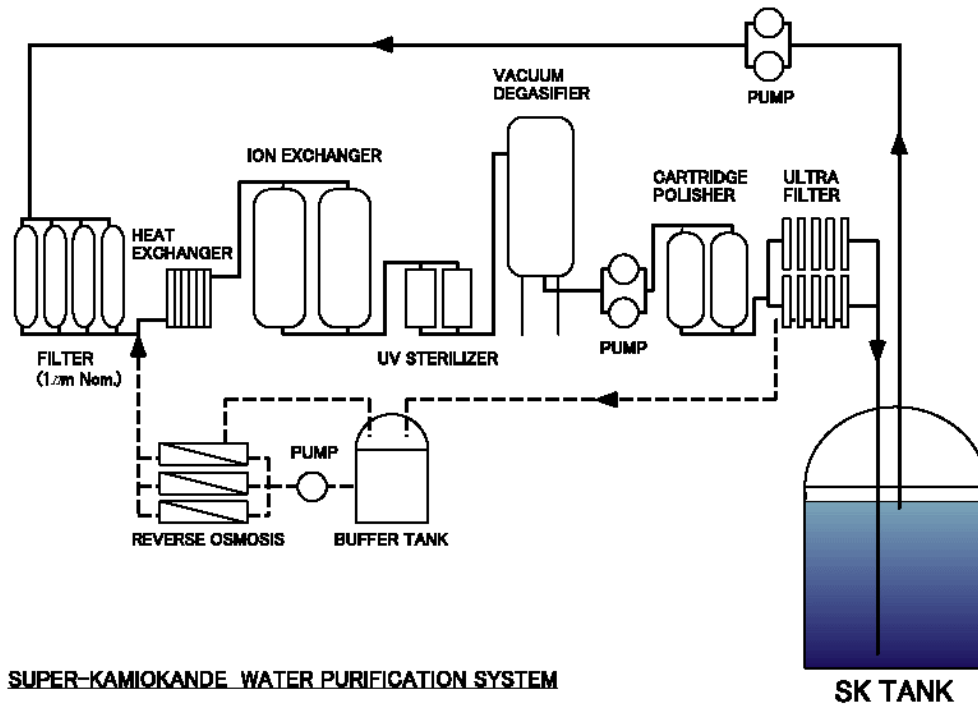


Figure 3.7: Schematic view of water purification system.

arrival time of each PMT signal. Signals from 12 PMTs are fed to an ATM board. Figure 3.8 shows a block diagram of the ATM board. The PMT signal into the current splitter is divided into four signals. One of them is fed to the discriminator with the threshold level for each channel set to -1 mV, which corresponds to $1/4$ pe equivalent. When the PMT signal is above the threshold level, a "hit" signal with 200 ns width and 15 mV pulse height is asserted on the ATM front panel. The HITSUM signal, which is used to generate the global trigger signal, is the analog sum of all these 15 mV/Channel pulses. At the same time, either of the split signals, A or B, is held by a QAC (Charge to Analog Converter), and a TAC (Time to Analog Converter) starts to integrate constant current. If a global trigger is received, the information in the TAC/QAC is digitized and stored in internal memory buffers. Since, for each channel, TAC integration is started by the PMT signal itself, the arrival time of the signal can be inferred from the value of the integrated charge. A "self gate" chip generates start/stop signals for the TAC, the gate signal for QAC, and clear signals for both. Output signals from the TAC/QAC are fed to an ADC and digitized. There are two TACs and QACs for each channel so that events in rapid succession, such as muon followed by its decay electron, can be processed without dead-time.

Figure 3.9 shows a schematic view of the inner detector data acquisition (ID DAQ) system. There are total 946 ATM modules, located in four "quadrant huts". ATMs record ADC/TDC data of each PMT above threshold when a global trigger signal is asserted by the VME TRG (TRiGger)

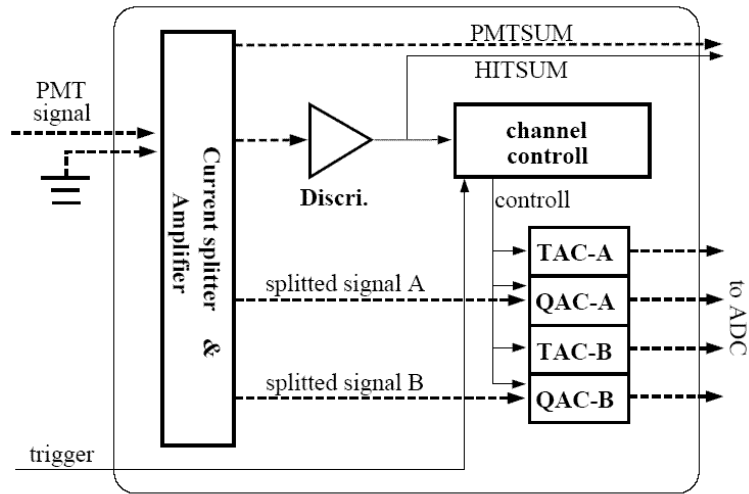


Figure 3.8: A block diagram of ATM board used for inner detector data acquisition.

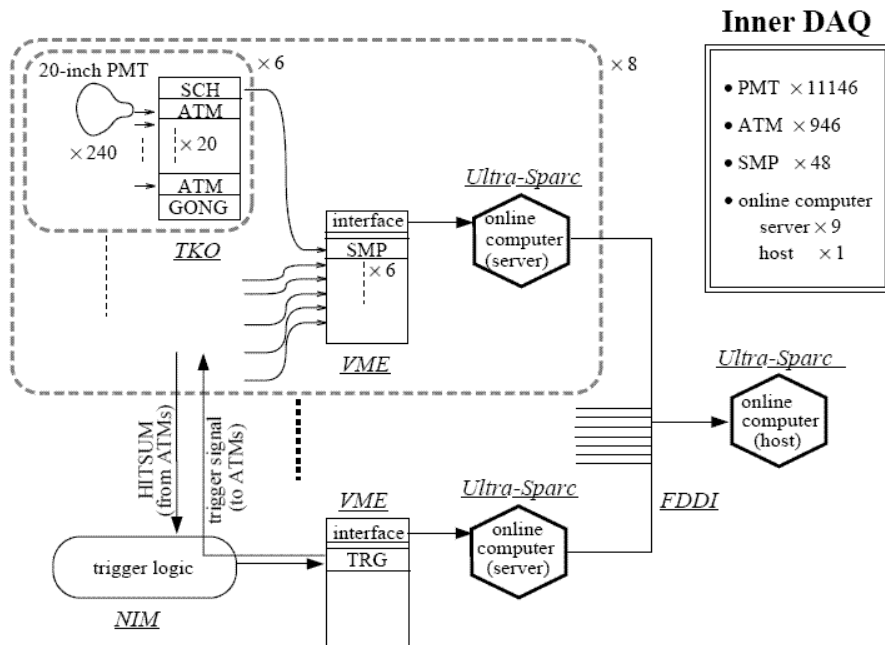


Figure 3.9: The data acquisition system for the inner detector.

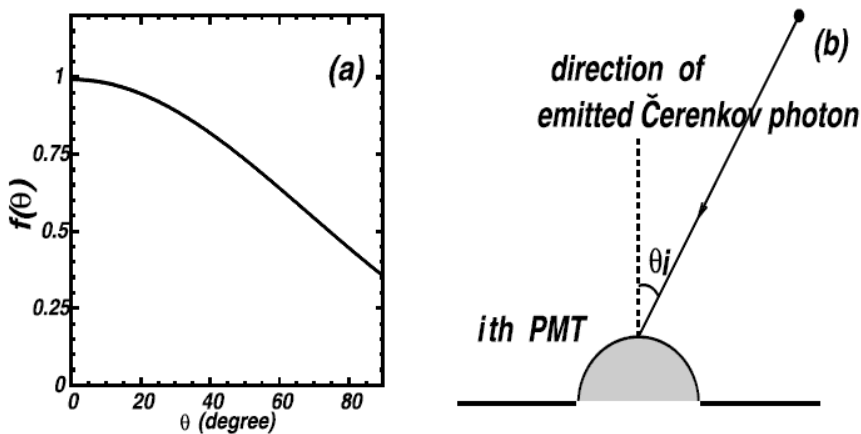


Figure 3.11: Relative photo-sensitivity. (a) Measurement result, (b) Definition of the incident angle.

3.3 Calibrations

3.3.1 Water Transparency Measurement

Indirect Measurement with Cosmic Rays

The light attenuation length in water can be measured by using through-going cosmic ray muons. These muons are energetic enough to deposit almost constant ionization energy per unit path length (about 2 MeV/cm) independent of particle energy. This fact makes it possible to use these muons as a "constant" light source. The advantage of this method is that continuous and abundant samples of muons come without cost as we take normal data. The disadvantage is that we cannot measure the transparency as a function of wavelength. However, since what we measure is the Cherenkov spectrum, this disadvantage is not necessarily a problem. Under the assumption that light reaching the PMTs is not scattered, the charge Q observed by a PMT is expressed by

$$Q = Q_0 \frac{f(\theta)}{l} \exp\left(-\frac{l}{L}\right) \quad (3.4)$$

Where l is the light path length, L the effective attenuation length, Q_0 a constant and $f(\theta)$ the relative photo-sensitive area, which depends upon the incidence angle θ of the light on the PMT, as shown in Figure 3.11. Figure 3.12 is as a function of the path length l together with the best fit in the form of the function defined above. The resulting attenuation length is found to be 105.4 ± 0.5 m.

As the data sample for this measurement is accumulated automatically while we take normal data, it is possible to continuously monitor the attenuation length as a function of time. Figure 3.13 shows the attenuation length changes with time, which are correlated with water quality. Such time variations in the attenuation length are corrected in analysis from the time series of calibration data.

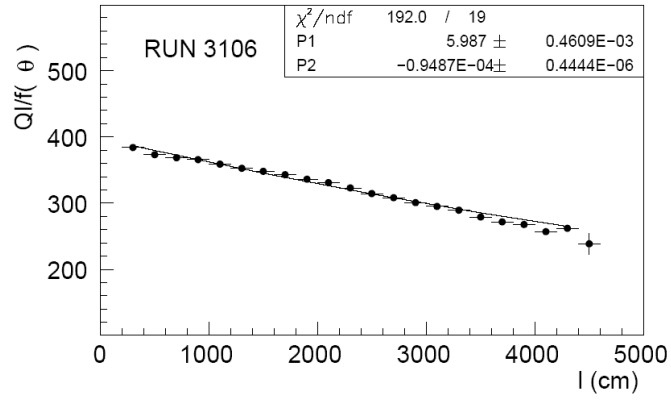


Figure 3.12: Effective charge observed as a function of the path length.

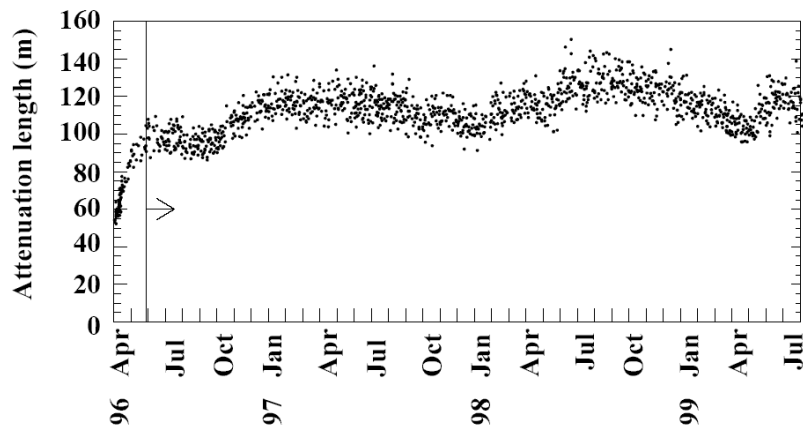


Figure 3.13: Time variation of the water attenuation length measured by through-going.

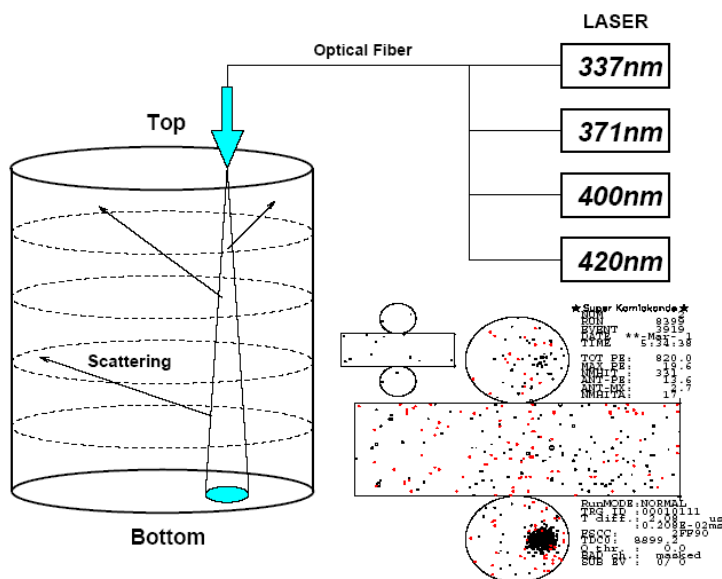


Figure 3.14: Laser system for water scattering and absorption parameter measurement and its typical events display.

Light Scattering Measurement with Laser

To measure the scattering and absorption parameters separately, a combination of dye and N2 lasers of wavelengths 337, 371, 400, 420 nm are used as light sources. In Super-Kamiokande I, the laser beam is brought into the top of the detector via optical fibers. Each laser fires every 6 second during normal data taking. Figure 3.14 shows a schematic view of the laser calibration setup and a typical event of laser light. A cluster of hits at the bottom of the tank is due to unscattered photons. The remaining hits, in barrel and top PMTs, are due to photons scattered in the water or reflected by the bottom PMTs and black sheet. The total charge in the cluster of bottom hits is used for normalization factor as a reference of light intensity. Figure 3.15 shows distributions of photon arrival times at the top PMTs. In the upper plot, the peak near 730 ns is from scattered photons, and the second peak represents reflected photons at the bottom of the detector. For the Monte Carlo, the total number of scattered photons is tuned using the scattering parameters, and the shape of the arrival time distribution is used to adjust the absorption parameters. The lower plot in Figure 3.15 shows the time dependence of the ratio between Monte Carlo and data, which agree within 2%. Using the measured absorption and scattering parameters, the light attenuation length of water is calculated using the following equation.

$$L_{attenu} = \frac{1}{\alpha_{abs} + \alpha_{scatt}} \quad (3.5)$$

Figure 3.16 compares the time variation of the light attenuation length measured by the 420 nm laser and cosmic ray muon during Super-Kamiokande I period. The result from cosmic ray muon is with average Cherenkov spectrum so it does not agree with the one from the laser system. However,

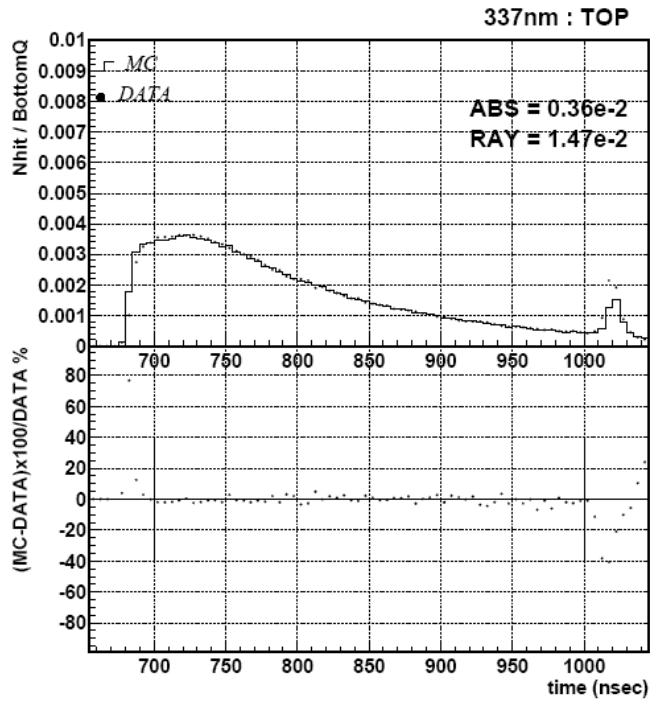


Figure 3.15: The upper plot is the photon arrival time distribution of the top PMTs. Dots is data and line is Monte Calro. The lower plot is the ratio, $(MC-DATA) \times 100 / DATA$.

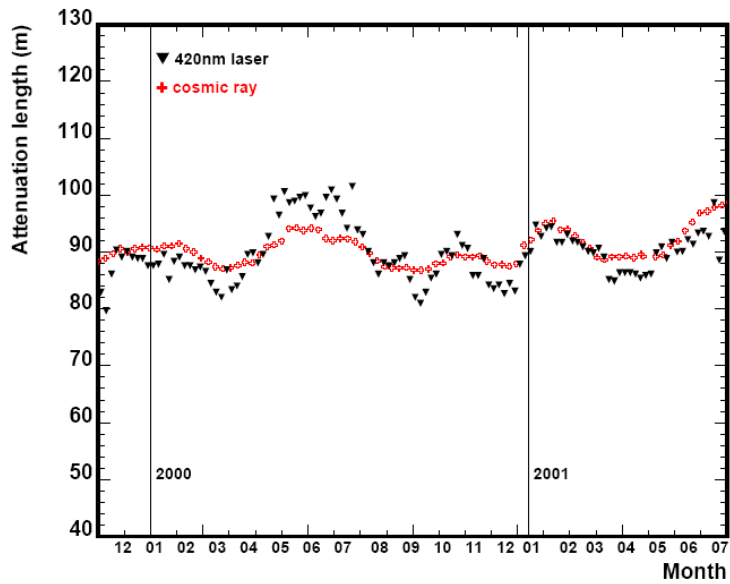


Figure 3.16: Time variation measured light attenuation length since November 1999, using the laser system (triangles) and cosmic ray muons (crosses).

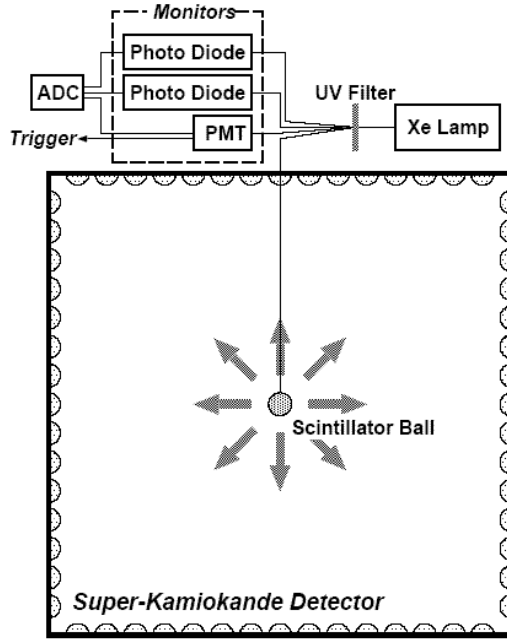


Figure 3.17: The relative gain measurement system.

we can see the tendency of time variation is consistent between the two measurements.

3.3.2 Relative Gain Calibration

The high voltage of each PMT is set to provide approximately equal gain for all PMTs in the Super-Kamiokande detector. Each PMT came with a nominal high voltage value, which was specified by Hamamatsu Photonics just after its production, using three calibration light sources : a DC light source, a Xe-lamp pulsed light source, and a light source at the single pe level. However, because of possible long-term drift in the factory calibration system, which may have caused a systematic difference between tubes manufactured at different times, all PMTs had their gain re-calibrated. Normalized Relative gain was measured by the system shown in Figure 3.17. Light generated by a Xe lamp is passed through an ultraviolet (UV) filter and injected into a scintillator ball via an optical fiber. The scintillator ball is an acrylic ball with BBOT (2, 5-bis(5'-tert-butyl-2-benzoxazolyl)thiophene) wavelength shifter and MgO powder diffuser. BBOT absorbs UV light and emits light with a peak at 440 nm, which is in the sensitive region of the PMTs used for Super-Kamiokande for Cherenkov light detection. In this measurement, each PMT detects a few tens of pe.

The intensity of the primary UV light is monitored by two photodiodes and one PMT. The output of the monitor PMT is also used for triggering. The relative gain G_i of the i -th PMT is obtained by

$$G_i = \frac{Q_i}{Q_0 f(\theta)} \cdot l_i \cdot \exp\left(\frac{l_i}{L}\right) \quad (3.6)$$

where Q_i is the observed charge by the PMT, Q_0 a constant, L the effective

light attenuation length, l_i the distance from the light source to the PMT and $f(\theta)$ the relative photo-sensitivity as a function of the incident angle of light a on the PMT defined in Figure 3.11. The high voltage value for each PMT is set so that the "corrected Q" of each PMT is approximately the same as for all the others. Here, "corrected Q" is the pulse height corrected for light attenuation, acceptance of the PMT, and uniformity of the scintillator ball. It is further normalized by the Xe monitor pulse height. This measurement is done for various positions of the scintillator ball and settings of the high voltage value. After the initial gain adjustment, long term stability of PMT gain was monitored using the same system. The absolute value of PMT gain cannot be measured while the experiment is running. The relative gain spread gain is defined as the standard deviation obtained by fitting the relative gain distribution of all PMTs to a Gaussian. It was 7.0% at the beginning of Super-Kamiokande I.

3.3.3 Relative Timing Calibration

The relative timing of PMT hits is important for event reconstruction. It depends on the length of the signal cable between the PMT and the ATM, and also depends on observed charge because of the discriminator slewing effect. The timing difference in each individual PMT has to be measured precisely to get better timing resolution. Figure 3.18 shows the system for measuring the relative timing of hit PMTs. The N2 laser emits intense light of wavelength 337 nm within a very short time (less than 3 ns). The wavelength is shifted to 384 nm, which is near the lower edge of sensitivity of a PMT to the Cherenkov light, by a dye laser module. The light intensity is changed by an optical filter, and the PMT timing is measured at various pulse heights. After passing through the optical filter, the light goes to the diffuser ball in the detector through an optical fiber. The schematic view of the diffuser ball is also shown in Figure 3.18. The diffuser tip located at the center of the ball is made from TiO₂ suspended in optical cement. The light emitted from the tip is further diffused by LUDOX manufactured by Grace Davison, silica gel made of 20 nm glass fragments. The combination of diffuser tip and LUDOX make modestly diffused light without introducing significant timing spread. A typical scatter plot of the timing and pulse height is shown in Figure 3.19, which is called a 'TQ-map'. Each PMT has its own TQ-map, which is applied in data reduction. The timing resolution of PMTs as a function of pulse height is estimated from the TQ maps. Typical timing resolution at the single pe level is better than 3 ns.

3.3.4 Other Calibrations

There are other calibrations using stopping muon, neutral pion, LINAC, etc. The detail of the other calibrations can be found in [32].

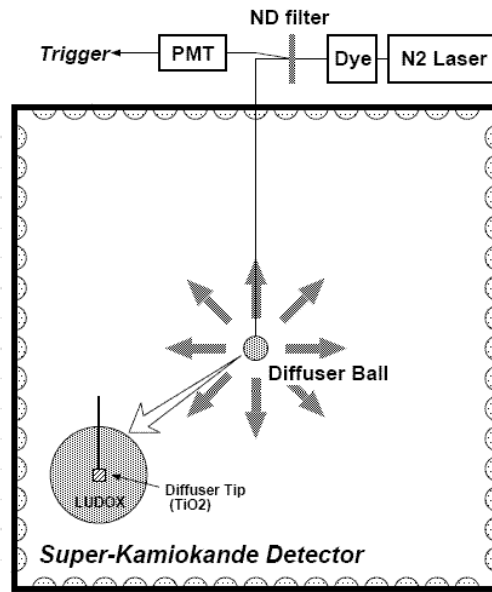


Figure 3.18: The timing calibration system.

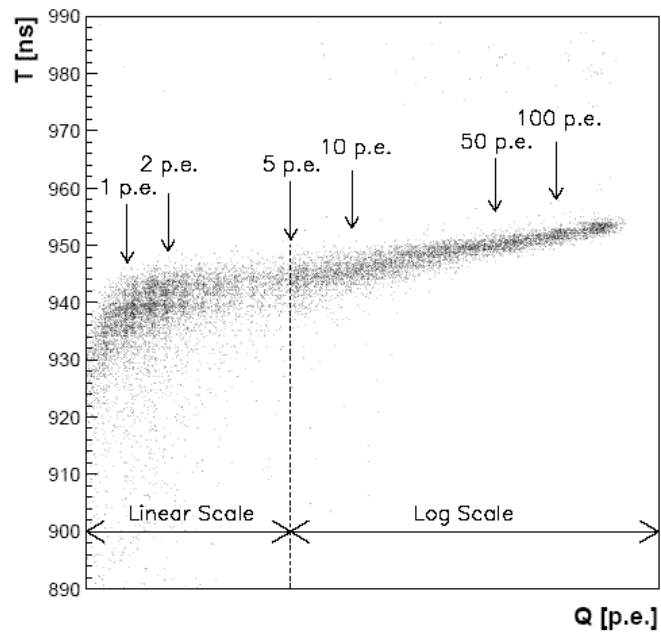


Figure 3.19: A typical plot of timing vs. pulse height. This plot is referred as 'TQ-map'.

Chapter 4

Simulation

We simulate not only the $n - \bar{n}$ oscillation but also the background events since background is pivotal component of a search for a rare process such as nucleon decay or transition. Atmospheric neutrino interactions with an average energy of 1~3 GeV are most significant source of background for $n - \bar{n}$ oscillation as well as nucleon decay. We use same 100 years atmospheric neutrino MC that has been used for neutrino oscillation study in Super-Kamiokande I of 4.07 years livetime. In this chapter, I outline the physical assumptions including those related to kinematics that are used in signal, background and detector response for $n - \bar{n}$ search.

4.1 $n - \bar{n}$ Oscillation

The $n - \bar{n}$ search focuses on possible oscillation and subsequent annihilation of neutrons bound in ^{16}O nuclei which are contained in H_2O molecules in the fiducial volume of Super-K detector. Thus, the kinematics that we should consider for this search is quite different from that of free neutrons due to Fermi motion that arises from the Pauli Exclusion Principle and nuclear effect described in terms of secondary particles such as pions. Our $n - \bar{n}$ simulation includes four phases.

1. Annihilation phase ($\sim 10^{-22}$ s): spontaneous oscillation and annihilation of neutron in a ^{16}O nucleus.
2. Pionization or mesonic phase ($\sim 10^{-18}$ s): production of the annihilation products.
3. Propagation phase ($\sim 10^{-12}$ s): propagation and possible decay of the annihilation products through the residual excited nucleus, ^{14}O or ^{14}N for annihilation of the \bar{n} on a n or p respectively.
4. Fragmentation phase ($\sim 10^{-8}$ s): decay and fragmentation of residual nucleus into nuclear fragments that include free neutrons, protons and isotopes of hydrogen and helium.

| channel | This analysis(%) | Cresti(1963)(%) | Baltay(1966)(%) |
|-----------------------------|-------------------|--------------------|--------------------|
| $\pi^+\pi^-$ | 2.(± 0.4) | 0.33(± 0.48) | 0.32(± 0.03) |
| $\pi^0\pi^0$ | 1.52(± 0.4) | 0. | 3.2(± 0.5) |
| $\pi^+\pi^-\pi^0$ | 6.48(± 0.7) | 5.4(± 0.7) | 7.8(± 0.90) |
| $\pi^+\pi^-2\pi^0$ | 11.(± 1.3) | 0. | * |
| $\pi^+\pi^-3\pi^0$ | 28.(± 1.3) | 0. | 34.5(± 1.2) |
| $2\pi^+2\pi^-$ | 7.(± 1.4) | 5.4(± 0.3) | 5.8(± 0.3) |
| $2\pi^+2\pi^-\pi^0$ | 24.(± 3.4) | 22.6(± 0.7) | 18.7(± 0.9) |
| $\pi^+\pi^-\pi^0\omega$ | 10.(± 0.9) | 0. | * |
| $2\pi^+2\pi^-2\pi^0$ | 10.(± 0.9) | 0. | 21.3(± 1.1) |
| $3\pi^+3\pi^-$ | 0. | 1.7(± 0.2) | 1.9(± 0.2) |
| $3\pi^+3\pi^-\pi^0$ | 0. | 1.7(± 0.2) | 1.6(± 0.3) |
| $3\pi^+3\pi^-m\pi^0(m > 1)$ | 0. | 0. | 0.3(± 0.1) |

* is the percent in this channel has been added to the percent in the below and result is reported in the line below.

Table 4.1: $\bar{n} - n$ annihilation branching ratio.

| channel | This analysis(%) | Bettini(1967)(%) |
|----------------------|------------------|--------------------|
| $\pi^+\pi^0$ | 1.(± 1.0) | ≤ 0.7 |
| $\pi^+2\pi^0$ | 8.(± 1.2) | * |
| $\pi^+3\pi^0$ | 10.(± 1.2) | 16.4(± 0.5) |
| $2\pi^+\pi^-$ | 0. | 1.57(± 0.21) |
| $2\pi^+\pi^-\pi^0$ | 22.(± 1.8) | 21.8(± 2.2) |
| $2\pi^+\pi^-2\pi^0$ | 36.(± 1.8) | 59.7(± 1.2) |
| $2\pi^+\pi^-\omega$ | 16.(± 4.0) | 12.0(± 3.0) |
| $3\pi^+2\pi^-\pi^0$ | 7.(± 4.0) | 23.4(± 0.7) |
| $4\pi^+3\pi^-m\pi^0$ | 0. | 0.39(± 0.07) |

Table 4.2: $\bar{n} - p$ annihilation branching ratio.

4.1.1 Annihilation and Pionization

An \bar{n} that is the product of spontaneous neutron oscillation is assumed to quickly annihilate with one of the remaining n or p in nucleus with probability of 46.7% and 53.3% respectively. These $\bar{n} - n$ and $\bar{n} - p$ annihilations are generated in the oxygen nucleus. Since the literature on \bar{n} annihilation in nucleus is meager, $\bar{p}p$ and $\bar{p}d$ data[36][37][38] from hydrogen and deuterium bubble chambers are used to determine the branching ratios for the annihilation final states, pionic phase. The branching ratios used in our simulation are summarized in Table 4.1 and are same as those used in the \bar{n} analysis of IMB[15]. The kinematics of this pionic phase are determined by relativistic phase-space including Fermi motion[39].

The \bar{n} annihilations are generated using two methods in $n - \bar{n}$ searches; A volume mode in which the nuclear matter density is uniform throughout the nuclear volume and annihilation vertices are thus uniformly distributed throughout the nuclear volume, and peripheral mode in which matter density increased as the nuclear surface is approached and thus annihilation vertices are more likely to be found near the nuclear surface. Our $n - \bar{n}$ simulation, as well as the most recent result in Soudan2, is based on volume mode which yields more conservative limit[14] although many of $n - \bar{n}$ searches adopted the peripheral distribution which were predicted by Dover et al.[40].

4.1.2 Pion Propagation

Produced pions from the \bar{n} annihilation are propagated through the excited residual nucleus before leaving the nucleus with a maximum total center of mass energy of 1850MeV and 1854MeV, which is the difference between the mass of an ^{16}O nucleus (16 AMU) and the mass of an ^{14}O or ^{14}N nucleus, for annihilation of an \bar{n} on a neutron and proton respectively.

This phase is simulated by a set of subroutines called "partnuc", which was written by Tegid W. Jones of IMB collaboration and has been modified for $n - \bar{n}$ analysis in Super-Kamioande. Figure 4.1 shows the relative starting position of the annihilation products in $n - \bar{n}$ simulation. Our simulation result labeled Partnuc is compared with that based on peripheral distribution predicted by Dover et al.. And consistency was checked with simulation result by nucleon decay MC in Super-K based on Wood-saxon, labeled "Eftrace". Eftrace is nuclear propagation program for nucleon decay and neutrino oscillation study in Super-K. The detail kinematics of nuclear propagation used in Super-K analysis is described in next section, Chapter 4.2.

The kinematics of our $n - \bar{n}$ simulation are basically same as that of IMB except for phase space distribution, our $n - \bar{n}$ simulation uses the routine called "genbod" from Cern Library for phase space distributions. It is assumed in this phase that the Δ resonance dominates, such that inelastic scattering proceeds by a pion interacting with a single bound nucleon to make a Δ resonance and that the Δ subsequently propagates through through nuclear matter. Provided that the Δ is not absorbed, the final result will be an inelastic or charge-exchange scattering. The cross sections for these two processes can be reasonably related to the corresponding elastic and charge-exchange cross sections of pions scattered of free protons that

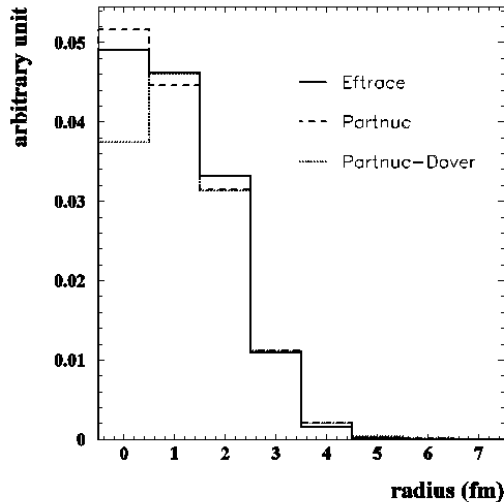


Figure 4.1: Relative position of annihilation in our simulation, labeled as Partnuc. Consistency is checked with Efrace used in nucleon decay study in Super-K and simulation based on peripheral distribution predicted by Dover is identical to others.

include the effects of Fermi-motion and Pauli blocking.

We assume pion-nucleon interactions depend linearly on nucleon density which is determined from electron-nucleon scattering data[41]. Finally the simulation results of pion-nucleon interactions inside the residual nucleus is checked using pion-oxygen data. Figure 4.2[15] compares the $\pi^{16}\text{O}$ cross sections deduced by IMB in 1983 using deuteron scaling and the $\pi^{16}\text{O}$ data interpolated from the pion-nucleus cross sections reported by Ashery et al.[42]. To make above agreement between the model predictions and the data, IMB made the following approximation. Absorption probability is taken to be $C\sigma_{\pi d}\rho^2$, where C is an adjustable parameter, $\sigma_{\pi d}$ is the πd cross section, and ρ is the local nuclear matter density. In our pion-nucleon simulation, we attempted to scale the pion absorption cross section by $\pi^{16}\text{O}$ instead of πd . This $\pi^{16}\text{O}$ cross section determined from $\pi^{16}\text{O}$ interactions used by Super-Kamiokande to simulate the interaction of π -mesons produced in nucleon decay. Our simulation result are plotted in Figure 4.3 and compared.

4.1.3 Fragmentation

The residual nucleus, $^{14}\text{N}^*$ after $\bar{n} - p$ and $^{14}\text{O}^*$ after $\bar{n} - n$ annihilation, decays and fragments to ^2H , ^3H , ^3He , ^4He , n, p and a remaining large nuclear fragment. The total energy of all of the daughter products from the annihilation and fragmentation must be equal to the mass of the original ^{16}O nucleus which is 16 AMU (=14,897 MeV). The final state of nuclear fragments is simulated in the fragmentation phase using an algorithm that we developed and a subroutine named by "nucfrag". Heavy isotopes of hydrogen and all isotopes of helium and larger nuclear fragments are removed before the Super-K detector simulation since all nuclear fragments other than free neutrons and protons give below Cherenkov threshold in detec-

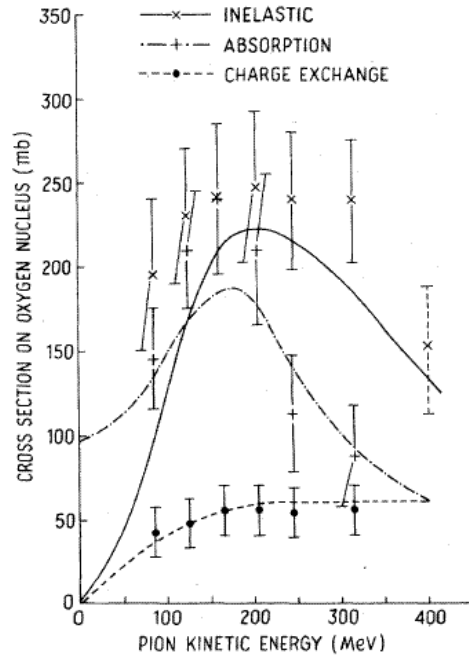


Figure 4.2: Comparison of interpolated data for pion- ^{16}O cross sections with the predictions of the IMB pion-nucleon interaction model obtained using deuteron scaling.

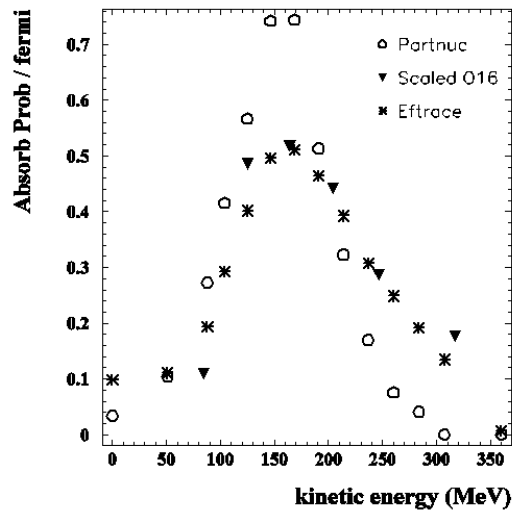


Figure 4.3: The absorption probability for pions within 3.5 fermi of the center of the nucleus. Partnuc, the IMB pion interaction program, is based on πd cross section and Efrace, the Super-K pion interaction program, is based on $\pi^{16}\text{O}$. Our simulation adopts "Scaled O16" which Partnuc was developed with scaled absorption probability.

tor simulation and Super-K detector simulation do not include these large nuclear fragments yet.

4.2 Atmospheric Neutrino

Atmospheric neutrino flux and interaction used in MC simulation are presented in detail in this section.

4.2.1 Neutrino Flux

There are several flux calculations. I outline the methods of the calculation and compare the results from three atmospheric neutrino flux calculations [43][44][45], which cover the energy range relevant to the present analysis, adopted in Super-Kamiokande I analysis. The flux from Honda et al.[44] is mainly used for Super-K analysis. Calculations start with primary cosmic ray based on measured fluxes, including solar modulation and geomagnetic field effects. The atmospheric neutrino MC is calculated for 3 years of solar minimum, 1 year of changing activity and 1 year of solar maximum according to the cosmic ray proton, helium and neutron measurements[46][47]. And the interaction of cosmic ray particles with the air nucleus, the propagation and decay of secondary particles are simulated. A neutrino flux was calculated specifically for the Kamioka site.

Energy Spectrum

The calculated energy spectra of atmospheric neutrinos at Kamioka are shown in Figure 4.4 (a). Figure 4.4 (b) compares the calculated fluxes as a function of neutrino energy. The agreement among the calculations is about 10% below 10 GeV. This can be understood because the accuracy in recent primary cosmic ray flux measurements[48][49] below 100 GeV is about 5% and because hadronic interaction models in each calculation are different. However the primary cosmic ray data is much less accurate above 100 GeV. Therefore, for neutrino energies much higher than 10 GeV, the uncertainties in the absolute neutrino flux could be substantially larger than the disagreement level among the calculations. Finally, the spectrum of primary cosmic ray is fitted with different index in the low energy (<100 GeV) and high energy (>100 GeV) region. Taking the flux weighted average of these spectrum index uncertainties, we assign 0.05 for the uncertainties in the energy spectrum index in the primary cosmic ray energy spectrum above 100 GeV.

Flavor Ratio

Figure 4.5 shows the calculated flux ratio of $\nu_\mu + \bar{\nu}_\mu$ to $\nu_e + \bar{\nu}_e$ as a function of the neutrino energy, integrated over solid angle. This ratio is essentially independent of the primary cosmic ray spectrum. Especially, in the energy region of less than about 5 GeV neutrino energies, most of the neutrinos are produced by the decay chain of pions and the uncertainty of this ratio is about 3%, which is estimated by comparing the three calculation results. In the higher energy region (10 GeV for $\nu_\mu + \bar{\nu}_\mu$, and 100 GeV for $\nu_e + \bar{\nu}_e$),

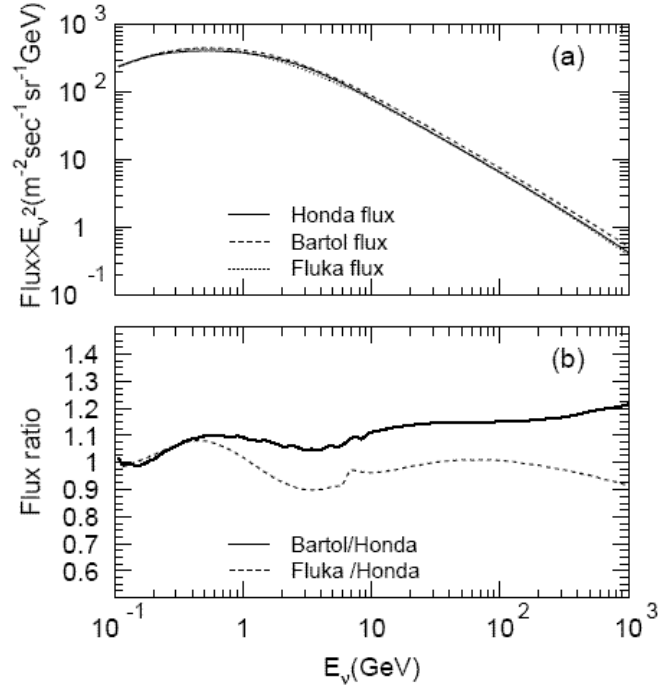


Figure 4.4: (a) The direction averaged atmospheric neutrino energy spectrum for $\nu_\mu + \bar{\nu}_\mu$ calculated by several authors are show by solid line[44], dashed line[43] and dotted line[45]. (b) The ratio of the calculated neutrino flux.

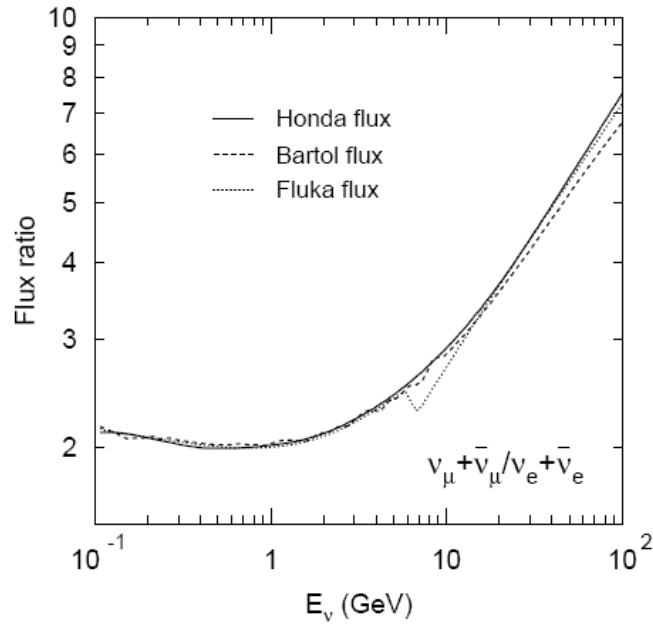


Figure 4.5: The flux ratio of $\nu_\mu + \bar{\nu}_\mu$ to $\nu_e + \bar{\nu}_e$.

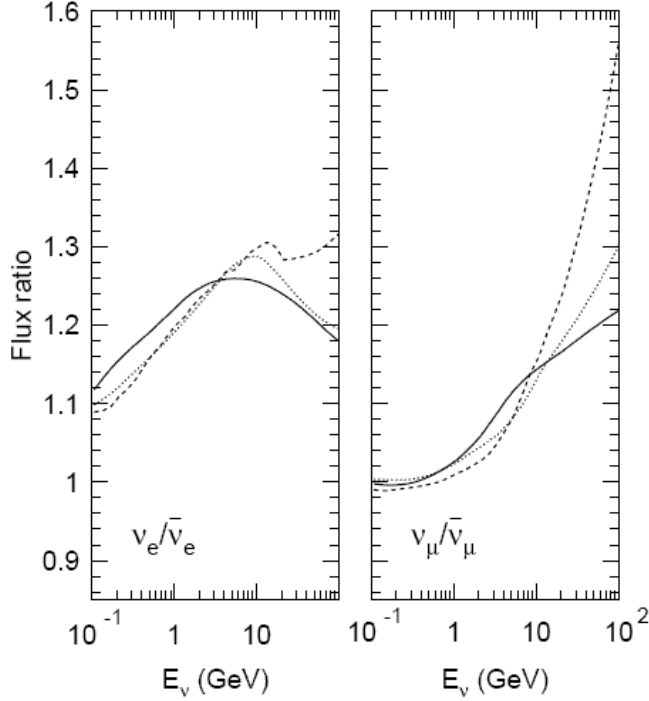


Figure 4.6: The flux ratio of ν_μ to $\bar{\nu}_\mu$ and ν_e to $\bar{\nu}_e$.

the contribution of K decay in the neutrino production is more important. There, the ratio depends more on the K production cross sections and the uncertainty of the ratio is expected to be larger. A 20% uncertainty in the K/π production ratio cause at least a few % uncertainties in the $\nu_\mu + \bar{\nu}_\mu$ to $\nu_e + \bar{\nu}_e$ ratio in the energy range of 10 to 100 GeV. However, as seen from Figure 4.5, the difference in the calculated $\nu_\mu + \bar{\nu}_\mu$ to $\nu_e + \bar{\nu}_e$ ratio is substantially larger than that expected from the K/π uncertainty in the high energy region. The reason for this difference has not been understood yet. As a consequence, an energy dependent uncertainty for the $\nu_\mu + \bar{\nu}_\mu$ to $\nu_e + \bar{\nu}_e$ ratio above 5 GeV neutrino energy is assumed based on the comparison of the three flux calculations. It is taken to be 3% at 5 GeV and 10% at 100 GeV.

$\nu/\bar{\nu}$ Ratio

Figure 4.6 shows the calculated flux ratios of ν_μ to $\bar{\nu}_\mu$ and ν_e to $\bar{\nu}_e$. The calculations agree to about 5% for both of these ratios below 10 GeV. However, the disagreement gets larger above 10 GeV as a function of neutrino energies. The systematic errors in the neutrino over anti-neutrino ratio are assumed to be 5% below 10 GeV and linearly increase with $\log E_\nu$ to 10% and 25% at 100 GeV, for the ν_e to $\bar{\nu}_e$ and ν_μ to $\bar{\nu}_\mu$ ratios, respectively.

Horizontal/Vertical Ratio and Up/Down Ratio

Figure 4.7 shows the zenith angle dependence of the atmospheric neutrino fluxes for several neutrino energies. At low energies, and at the Kamioka

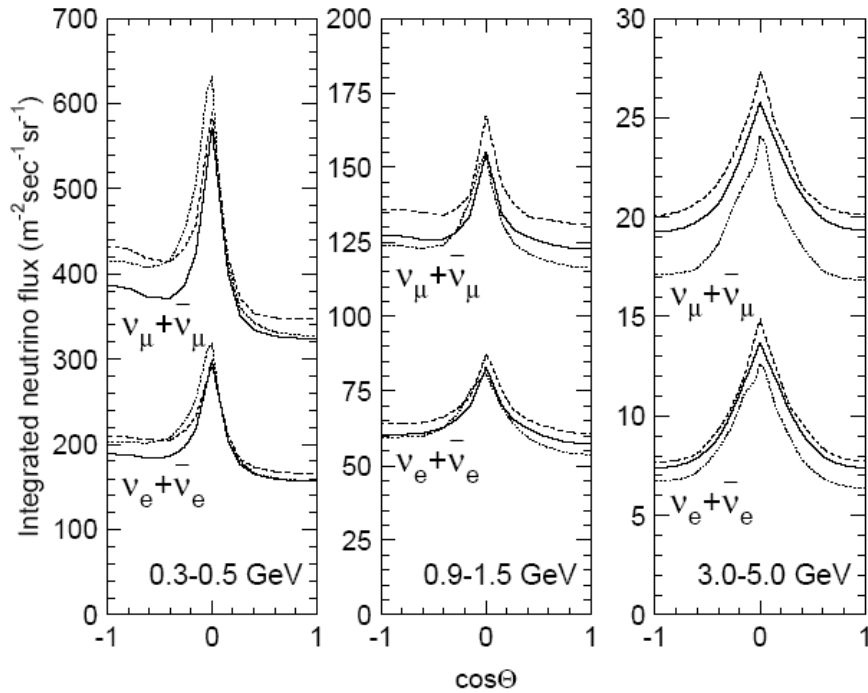


Figure 4.7: The flux of atmospheric neutrinos v. zenith angle.

location, the fluxes of downward-going neutrinos are lower than those of upward-going neutrinos. This is due to the deflection of primary cosmic rays by the geomagnetic field, roughly characterized by a minimum rigidity cutoff. For neutrino energies higher than a few GeV, the calculated fluxes are essentially up-down symmetric, because the primary particles are more energetic than the rigidity cutoff.

One of the feature characteristics of full three dimensional flux calculations is the enhancement of the flux near horizon for low energy neutrinos. However, in Super-Kamiokande, the horizontal enhancement cannot be seen in the lepton zenith angle distribution, due to the relatively poor angular correlation between neutrinos and leptons below 1 GeV. The uncertainties in the up-down and vertical-horizontal ratios of the number of events are estimated by comparing the predicted ratios of various flux models. These uncertainties generally depend on the energy and the neutrino flavor. The uncertainty in the up-down event ratio is about 1 to 2% in the sub-GeV energy region and is about 1% in the multi-GeV energy region. The main source of the uncertainty in the vertical-horizontal ratio around a GeV is the size of the horizontal enhancement of the flux due to the three dimensional effect; the uncertainty is estimated to be less than a few percent. In the higher energy region, where upward through-going muons are relevant, the largest source of the uncertainty in the vertical-horizontal ratio is the K/π production cross section. We assume that the K/π production ratio uncertainty is 20% in the whole energy region. The uncertainties in the zenith angle and energy distributions due to the K/π production uncertainty are included in the systematic errors in the analysis. This error is most important for higher energy neutrinos. For example, the vertical-horizontal uncertainty

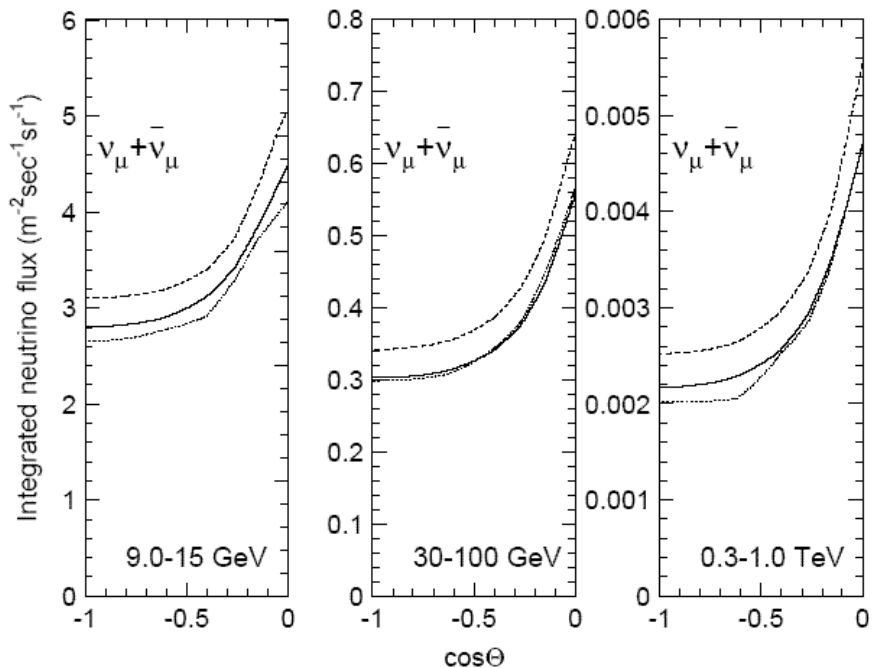


Figure 4.8: The flux of upward-going atmospheric neutrinos vs. zenith angle for higher energy region.

for upward through-going muons due to the K/π production uncertainty is estimated to be 3% [50]. Figure 4.8 shows the zenith angle dependence of the atmospheric neutrino fluxes for higher energy region observed as upward muons in Super-Kamiokande.

In summary of the atmospheric neutrino flux, we remark that, the $\nu_\mu + \bar{\nu}_\mu$ to $\nu_e + \bar{\nu}_e$ ratio is predicted to an accuracy of about 3% in the energy region relevant to the data analysis discussed in this thesis. The zenith angle dependence of the flux is well understood, and especially, above a few GeV neutrino energies, the flux is predicted to be up-down symmetric.

4.2.2 Neutrino Interactions

The simulation of neutrino interactions relies on detailed comparison of the experimental data with the theoretical expectation. An important element of this is to simulate the interaction of neutrinos from 10 MeV to 100 TeV with the nuclei of water, or in the case of upward going muon, the nuclei of the rock surrounding the detector, assumed to be SiO_2 . Two simulation programs, NEUT and NUANCE, are available for neutrino interaction. In this section, one of models (NEUT) is described. This program was developed to study atmospheric neutrino and nucleon decay in Kamiokande [51] and has been continuously updated for Super-Kamiokande. In the simulation program, the following interactions were considered.

- quasi elastic scattering $\nu N \rightarrow lN'$
- single meson production $\nu N \rightarrow lN'm$

- coherent π production $\nu^{16}O \rightarrow l\pi^{16}O$
- deep inelastic scattering $\nu N \rightarrow lN'hardron$

Where, N and N' are the nucleons, l is the lepton, and m is the meson, respectively.

Elastic and Quasi-Elastic Scattering

The cross section of quasi-elastic scattering off a free proton, which was used in the simulation programs, was described by Llewellyn-Smith[52]. For the $\nu^{16}O$ scattering, the Fermi motion of the nucleons and Pauli Exclusion Principle are taken into account. The nucleons are treated as quasi-free particles using the relativistic Fermi gas model of Smith and Moniz[53]. The momentum distribution of the nucleons were assumed to be flat up to the fixed Fermi surface momentum of 225 MeV/c. This Fermi momentum distribution was also used for other nuclear interactions. The nuclear potential was set to 27 MeV/c.

Single Meson Production

To simulate the resonance productions of single π , K and η , Rein and Sehgal's model[54][55] was adopted. In this model, the interaction is separated into two parts as follows.

$$\begin{aligned}\nu N &\rightarrow lN^* \\ N^* &\rightarrow mN'\end{aligned}$$

where m is a meson, N and N' are nucleons, and N^* is a baryon resonance. To obtain the cross sections, we calculate the amplitude of each resonance production and then multiply the probability of decay into one pion and nucleon to each resonance. In order to avoid double counting of interaction, the hadronic invariant mass, W (the mass of the intermediate baryon resonance), is restricted to be less than 2 GeV/ c^2 . In addition to the dominant single π production, K and η production is considered. To determine the angular distribution of pions in the final state, Rein and Sehgal's method for the $P_{33}(1232)$ resonance were used. For the other resonances, the directional distribution of the generated pions is set to be isotropic in the Adler Frame (resonance rest frame). The angular distribution of π^+ has been measured for $\nu p \rightarrow \mu^- p \pi^+$ mode[56] and the results agree well with the Monte Carlo prediction. The Pauli blocking effect in the decay of the baryon resonance was considered by requiring that the momentum of nucleon should be larger than the Fermi surface momentum. Pion-less delta decay is also considered, where 20 % of the events do not have the pion and only the lepton and nucleon are generated[57].

There is a parameter that should be determined by experiment in the quasi-elastic scattering and single meson production. The parameter is called axial vector mass, M_A . For larger M_A values, interactions with higher Q^2 values (and therefore larger scattering angles) are enhanced for these channels. The M_A value was tuned using the K2K[58] near detector data. In our atmospheric neutrino interaction Monte Carlo simulation, M_A was

set to 1.1 GeV for both the quasi-elastic and single meson production channels, but the uncertainty of the value is estimated to be 10%. Coherent single pion production, the interaction between the neutrino and the entire oxygen nucleus, was simulated using the formalism developed by Rein and Sehgal[59].

Deep Inelastic Scattering

The cross sections of deep inelastic scattering was calculated using the GRV94[60] for the nucleon structure function. In the calculation, the hadronic invariant mass, W , is required to be greater than 1.3 GeV/ c^2 . And for actual calculation, we use the probability function of pion multiplicity, which is a function of W region ($W \leq 2\text{GeV}/c^2$). The multiplicity of pions is restricted to be greater than or equal to 2 for $1.3 < W < 2.0\text{GeV}/c^2$, because single pion production is separately simulated as previously described. In order to generate events with multi-hadron final states, two models were used. For W between 1.3 and 2.0 GeV/ c^2 , a custom made program[61] was used to generate the final state hadrons; only pions are considered in this case. For W larger than 2 GeV/ c^2 , PYTHIA/JETSET[62] was used. Total charged current cross sections including quasi-elastic scattering, single meson productions and deep inelastic scattering are shown in Figure 4.9.

Nuclear Effect

The interactions of mesons and nucleons, which are generated in ^{16}O nucleus, are also important for the atmospheric neutrino interaction and nucleon decay. This process is simulated by a subroutine named "eftrace". In Chapter 6, this program is tested for systematic uncertainty of nuclear propagation in $n - \bar{n}$ search. Basically, all of the interactions were treated by using a cascade model. The interactions of pions are very important because the cross section for pion production is quite large for neutrino energies above 1 GeV and the interaction cross sections for pions in nuclear matter is also large. In the simulation of pion interactions in ^{16}O , inelastic scattering, charge exchange and absorption were considered. The procedure to simulate these interactions is as follows. The initial position of the pion was generated according to the Woods-Saxon nucleon density distribution[63]. The interaction mode is determined from the calculated mean free path of each interaction. To calculate the mean free path, the model described by Oset et al.[64] was adopted. The calculated mean free path depends not only on the momentum of pion but also on the position of the pion in the nucleus. If inelastic scattering or charge exchange occurs, the direction and momentum of the pion are determined by using the results of a phase shift analysis obtained from $\pi - N$ scattering experiments[65]. In calculation of the pion scattering amplitude, the Pauli blocking effect is also taken into account by requiring the nucleon momentum after interaction to be larger than the Fermi surface momentum ($P_F(r)$) at the interaction point defined as follows.

$$P_F(r) = \left[\frac{3}{2} \pi^2 \rho(r) \right]^{-\frac{1}{3}} \quad (4.1)$$

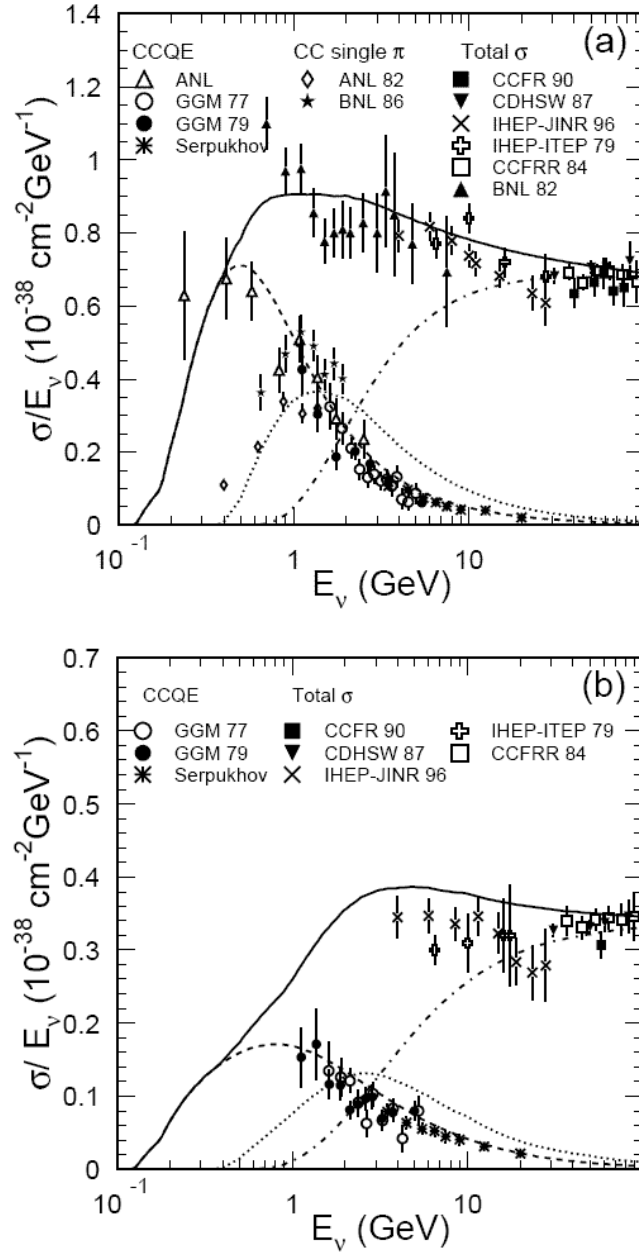


Figure 4.9: Charged current total cross section divided by E_ν for (a) neutrino and (b) anti-neutrino nucleon charged current interactions. Solid line shows the calculated total cross section. The dashed, dot and dash-dotted lines show the calculated quasi-elastic, single-meson and deep-inelastic scattering, respectively.

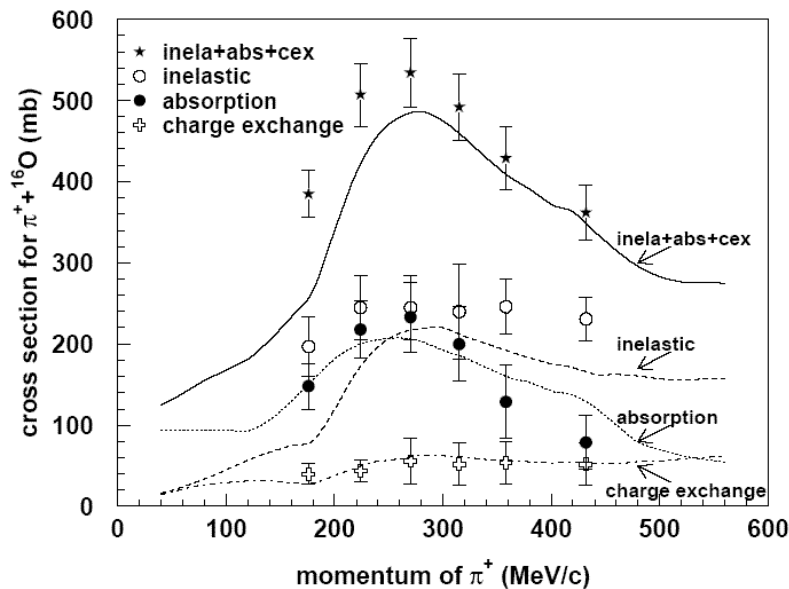


Figure 4.10: The cross section of $\pi^{16}O$ interactions. The lines show the results of our calculation based on [64] and the points show experimental data[66].

$$\rho(r) = \frac{Z}{A} \bar{\rho} \frac{1}{1 + \exp(\frac{|r|-c}{a})} \quad (4.2)$$

where $A(=16)$ is mass number, $Z(=8)$ is atomic number, $\bar{\rho}(=0.48 m_{\pi}^3)$ is average density of nucleus, $a(=0.41 \text{ fm})$ and $c(=2.69 \text{ fm})$ are density parameters of oxygen nucleus, respectively. The pion interaction simulation was checked using data for the following three interactions: $\pi^{12}C$ scattering, $\pi^{16}O$ scattering and pion photo-production($\gamma + ^{12}C \rightarrow \pi^{-} + X$)[66]. One of comparison is shown in Figure 4.10.

4.3 Detector Simulation

The particles left the oxygen nucleus after anti-neutron annihilation or neutrino interactions are fed into a detector simulation code. The simulation program includes the tracks of particles, Cherenkov radiation, propagation of Cherenkov photons in water and the response of PMTs and the readout electronics. The detector simulator program has been developed based on GEANT package[67]. The program simulates the tracks of particles, Cherenkov radiation, propagation of Cherenkov photons in water, and the response of PMTs and the readout electronics. And various processes for each particles are considered in our simulation program as listed in Table 4.3.

When a π^0 escapes from the oxygen nucleus or a π^0 is generated by free proton interaction, it immediately decays to two gammas (98.8% branching ratio). However, since π^{\pm} has relatively long lifetime, the propagation of π^{\pm} in water should be simulated. CALOR package[68] is employed in our simulation code. This package is known to reproduce the pion interactions

| | |
|-----------|---|
| γ | (e^+, e^-) pair production Compton scattering Photoelectric effect |
| e^\pm | Multiple scattering Ionization and γ -rays production Bremsstrahlung Annihilation of positron Generation of Cherenkov radiation |
| μ^\pm | Decay in flight Multiple scattering Ionization and γ -rays production Bremsstrahlung Direct (e^+, e^-) pair production Nuclear interaction Generation of Cherenkov radiation |
| Hadrons | Decay in flight Multiple scattering Ionization and γ -rays production Hadronic interactions Generation of Cherenkov radiation |

Table 4.3: List of the processes considered in simulator

well including low energy region (1 GeV/c). For still lower energy region ($p_\pi \leq 500$ MeV/c), a custom program[69] based on experimental data from $\pi - {}^{16}\text{O}$ scattering[70] and $\pi - P$ scattering[71] is used in our simulation code.

The Cherenkov photons are generated according to the Eq. (3.2) and (3.3). For the propagation of Cherenkov photons in water, Rayleigh scattering, Mie scattering and absorption are taken into account. According to the size of target particles, the interaction types are assigned[72]. Attenuation coefficients by Eq. (3.5) used in our simulation are shown in Figure 4.4, which are tuned to reproduce the measurement using laser system (Chapter 3.3.1).

Light reflection and absorption on detector material, such as the surface of PMTs and black sheets, are also simulated using probability functions that depend on the photon incident angle estimated from direct measurements.

For the simulation of the PMT response, measured quantum efficiency is used. The total amount of p.e.s detected in each PMT is derived by summing up individual p.e. with a weight of a single p.e. distribution. The hit time of each PMT is smeared according to the PMT timing resolution. Properties of the electronics system, such as the time width of ADC gate and the signal threshold, are also taken into account.

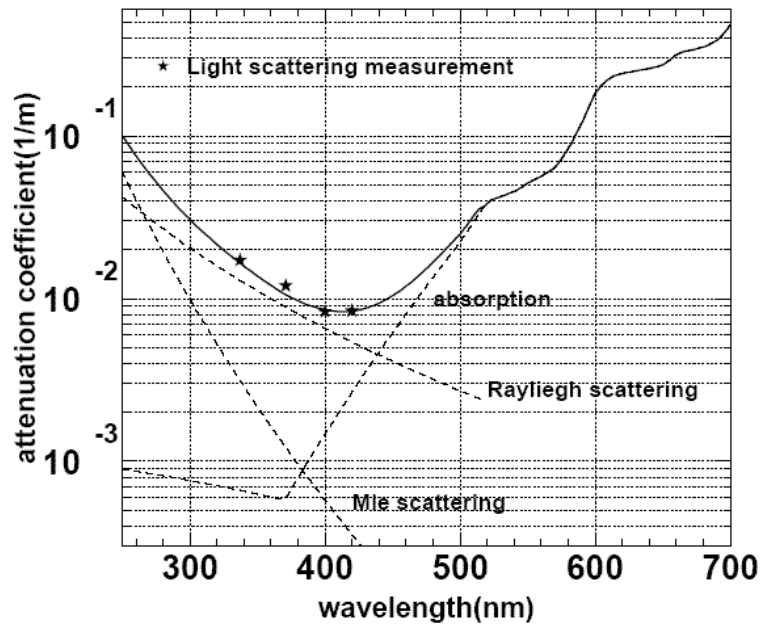


Figure 4.11: Wavelength dependence of attenuation coefficient (L_{attenu}^{-1}) obtained by light scattering measurement. Point is measurement in Chapter 3.3.1.

Chapter 5

Data Reduction and Reconstruction: Fully-Contained Events

The Super-Kamiokande I data was acquired from May, 1996 to July, 2001. The data are classified into three groups; fully-contained (FC), partially-contained (PC) and upward-going muons (UPMU). To separate FC and PC events, a fast spatial clustering algorithm is applied to the outer detector hits; if the number of hits in the largest OD cluster is less than 10, the events is defined as fully-contained. Otherwise, it is defined as partially-contained. The neutrino energies of partially-contained events are typically 10 times higher than that of fully-contained. Figure 5.1 shows the separation.

The analyses using these two data sets are based on independent data reduction and reconstruction. This section outlines the programs for reduction and reconstruction for fully-contained data which is used in atmospheric neutrino and nucleon decay (including $n - \bar{n}$ search) analysis. These same programs are also applied to atmospheric neutrino MC and $n - \bar{n}$ MC.

5.1 Data Reduction

The Super-Kamiokande has been taking the data with the trigger rate of 10 Hz every day except for 10% down time due to detector calibration, maintenance of detector and so on. 2.7 Hz are due to cosmic ray muon and 6 Hz are due to relatively low energy (a few MeV) events caused by radioactivity in the detector water or gamma rays from surrounding PMTs and rocks. Remaining 1 Hz are due to fake triggers caused by reflection of PMT signals and unwanted PMT signals following highly energetic events (so-called "after pulsing"). Therefore, we should eliminate these background to find the possible $n - \bar{n}$ events from the cosmic ray events. Cosmic ray muons are easily discriminated by requiring little or no ring activity in the outer detector. For atmospheric neutrino and nucleon decay analysis, we consider the events with visible energy above 30 MeV where visible energy (Evis) is defined as the energy of an electromagnetic shower that gives a certain amount of Cherenkov light (for example, a muon of momentum 300 MeV/c yields a visible energy of about 110 MeV). To make the final FC

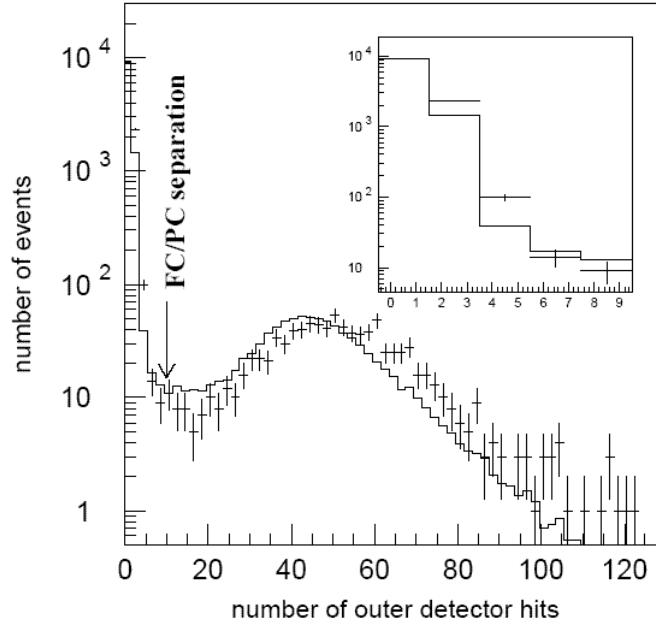


Figure 5.1: The number of hits in the largest outer detector cluster, which is used to separate the fully-contained and partially-contained event samples. The histogram shows the MC prediction with neutrino oscillation.

data sample, the following five steps of data reduction criteria are used.

5.1.1 1st and 2nd Reduction

Simple and efficient criteria are applied in the first and second reduction steps:

- $PE_{300} > 200$ p.e
Where, PE_{300} is the maximum total photo electrons collected in the inner detector within a 300 nsec sliding time window.
- $PE_{max}/PE_{300} < 0.5$
Where, PE_{max} is the maximum p.e. in any single ID PMT.
- $NHITA_{800} < 25$ hits
Where, $NHITA_{800}$ is the number of hit OD PMT within 800 nsec sliding time window.
- $TDIFF > 100\mu$ sec
Where $TDIFF$ is the time interval from the preceding event. This is to reject electrons from stopping muon decays.

5.1.2 Third Reduction

More complex criteria are applied in the third reductions step for further rejection of cosmic ray muons and low energy events:

- $NHITA_{in} < 10$ hits and $NHITA_{out} < 10$ hits
Where, $NHITA_{in}$ ($NHITA_{out}$) is the number of hit OD PMTs within

8 m from the entrance (exit) point of muon track fitted using the inner detector light pattern.

- $NHIT_{50} \geq 50$ hits

Where, $NHIT_{50}$ is the number of hit ID PMTs in 50 nsec sliding time window.

5.1.3 Fourth Reduction

Additional selection criteria are used to eliminate spurious events, such as "flashing" PMTs that emit light from internal corona discharges. Flasher events are removed by two different methods.

- Typical flasher events have broader PMT timing distributions than the neutrino events. Events with broader timing distributions are eliminated.
- Since flasher events have a tendency to be repeated with similar spatial hit distribution, the pattern information of observed charge is used on to eliminate these events. A correlation parameter based on the charge pattern is calculated with other data events and a "matched" tag is assigned for highly correlated events.

A cut is applied based on maximum correlation value and the number of "matched" with other events.

5.1.4 Fifth Reduction

Two further event types are eliminated in the fifth reduction step.

- $NHITA_{off} < 10$ hits

Where $NHITA_{off}$ is the number of OD hits in 200 nsec sliding time window preceding the trigger time (-8900 ~ -100 nsec). This cut eliminates decay electrons from invisible cosmic ray muons that are below Cherenkov threshold in the inner detector.

- Cosmic ray muons are removed using a more precise fitter and the same criteria as the first cut of (3).

Finally, the vertex is required to be within a fiducial volume (FV), 2 meters from the wall of the inner detector, and the visible energy is required to be greater than 30 MeV. Table 5.1 shows the event rate after each reduction step.

5.2 Reconstruction

The fully-contained events after passing through the data reduction, undergo reconstruction process.

| Reduction step | Data | Monte Carlo |
|------------------|---------------|--------------------|
| Trigger | 1,889,599,293 | 14,013.9 (100.00%) |
| First reduction | 4,591,695 | 14,006.3 (99.95%) |
| Second reduction | 301,791 | 14,006.1 (99.94%) |
| Third reduction | 66,810 | 13,993.3 (99.85%) |
| Fourth reduction | 26,937 | 13,898.1 (99.17%) |
| Fifth reduction | 23,984 | 13,895.3 (97.15%) |
| FV and Evis cuts | 12,180 | 13,676.7 (97.59%) |

Table 5.1: Number of events after each reduction for fully-contained events during 1489 days of the detector live-time. The Monte Carlo numbers and efficiencies down to the fifth reduction are for events whose real vertex is in the fiducial volume, the number of outer detector hits fewer than 10 and the visible energy larger than 30 MeV. In the last line, the fitted vertex is used for both data and Monte Carlo.

5.2.1 Vertex Fitting

The reconstruction process starts from vertex fitting. The vertex fitting consists of following three steps.

1. Point-fit : The point at which the timing residual distribution of hit PMTs has the sharpest peak is estimated.
2. Ring edge search : The direction and outer edge of the dominant ring is estimated by the Cherenkov opening angle expected from the charge within the cone.
3. TDC-fit : the track length of the charged particle and scattered Cherenkov photons are taken into account in the calculation of the time residual.

The vertex resolution is estimated to be 30 cm for single-ring fully-contained events. The vertex positions are more precisely estimated later by MS-fit using ring pattern.

5.2.2 Ring Counting

After a ring direction and vertex are roughly found through the previous vertex fitting algorithm, other possible rings are searched using a Hough transform[73] based technique. The technique is iterative. A second ring is searched for by choosing possible ring directions based on the Hough map, and a likelihood technique determined if a second ring from the list of the possible rings is more consistent with the data than just one ring. If a second ring is judged to be more consistent, then this procedure is repeated as many as necessary until finally no further rings are necessary to fit the data. Figure 5.2 shows the likelihood difference between the 2 ring assumption and a 1 ring assumption. In these figures, the oscillation at the best fit parameters ($\sin^2 2\theta = 1.0, \Delta m^2 = 2.1 \times 10^{-3} eV^2$) was taken into account for the Monte Carlo prediction. A cut was made at likelihood difference

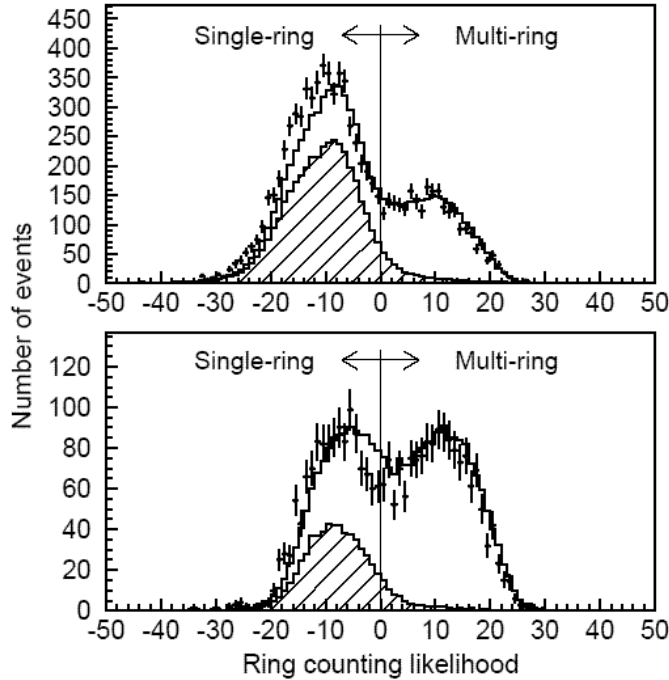


Figure 5.2: The distribution of the likelihood difference between a single-ring assumption and a multi-ring assumption for sub-GeV (top) and multi-GeV (bottom) FC events. The hatched histograms show the charged current quasi-elastic interactions.

of 0 to separate single and multi ring events. The efficiency for identifying charged current (CC) quasi-elastic $\nu_e(\nu_\mu)$ events as single-ring is 93.2 (95.8) % and the track's angular resolution for these single-ring events is estimated to be 3.0° and 1.8° for single-ring e -like and μ -like events, respectively. The detail description of this process can be found in [74].

5.2.3 Particle Identification

To determine the identity of the final state particles, a particle identification algorithm is applied which exploited systematic differences between Cherenkov rings produced from different particles. Cherenkov rings from an electron or gamma-ray exhibit diffuse light distribution because of electromagnetic cascades and multiple scattering and are called e -like events. On the other hand, Cherenkov rings from muon or charged pion give sharper ring edge and are called μ -like events. Figures 5.3 and 5.4 show observed single-ring e -like and μ -like events, respectively.

The opening angle of the Cherenkov cone, which depends on $\beta(\equiv v/c)$, is also used to separate e -like and μ -like events at low momenta. The validity of the method was confirmed by a beam test experiment at KEK[75]. The misidentification probabilities for single-ring e -like and μ -like events are estimated to be 0.8% and 0.7% respectively, using simulated charged CC (Charged Current) quasi-elastic neutrino events. The distribution of the likelihood variable used to discriminate single-ring e -like and μ -like events are shown for both the data and MC for the sub-GeV and multi-GeV sam-

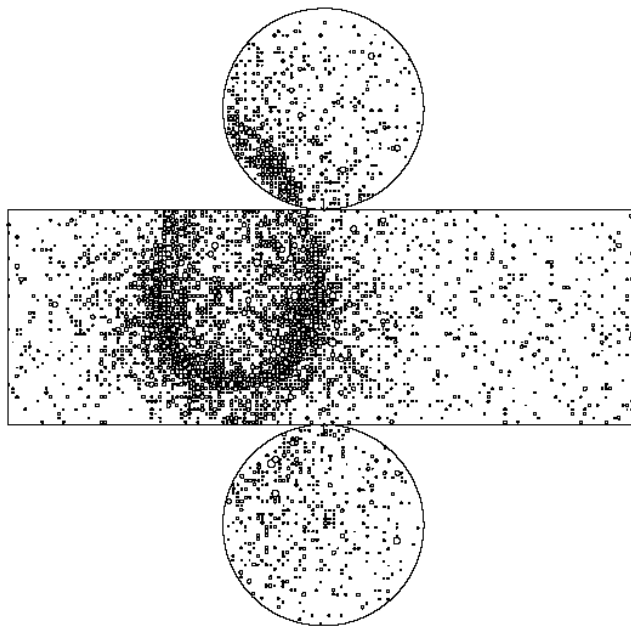


Figure 5.3: An event display of a single-ring e -like.

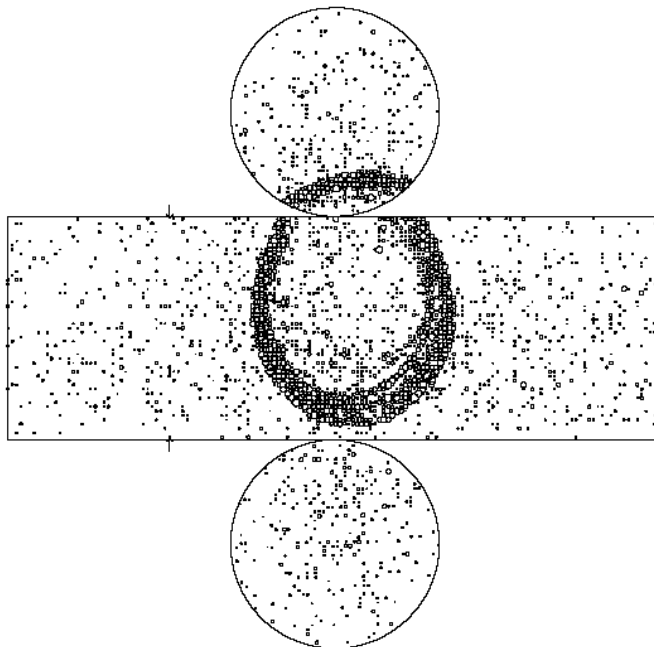


Figure 5.4: An event display of a single-ring μ -like.

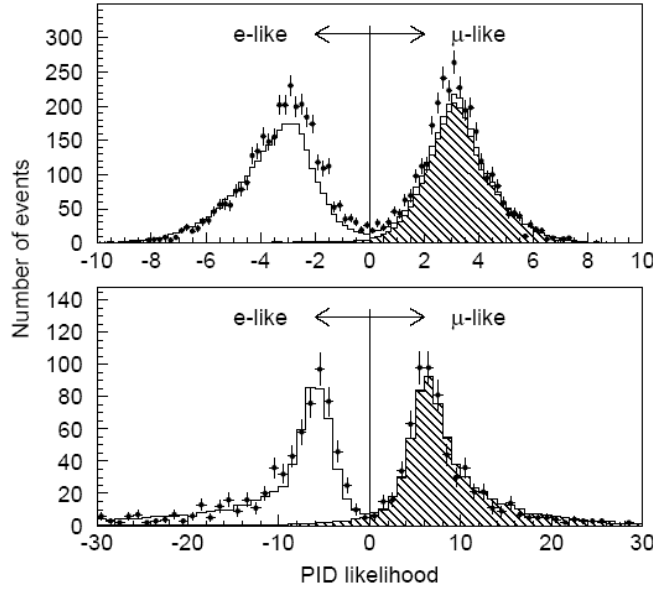


Figure 5.5: The distribution of particle identification likelihood for sub-GeV (top) and multi-GeV (bottom) FC single-ring events, comparing data (points) and atmospheric neutrino MC. The MC includes neutrino oscillation. The hatched histograms show the ν_μ charged current interactions.

ples in Figure 5.5. In both of these cases, the figures show a clear separation of the likelihood variable.

The identification efficiency is checked using cosmic ray muons that stop in the detector and subsequently decay to electrons. These events are easily selected by their timing signature. The resulting misidentification probabilities for stopping cosmic ray muons and decay electron light patterns are $0.4 \pm 0.1\%$ and $1.8 \pm 0.5\%$ respectively.

5.2.4 Precise Vertex Fitting and Momentum Determination

To obtain more precise vertex position, the vertex position is estimated by MS-fit for single-ring events taking into account the expected light pattern given by the particle identification. In the case of multi-ring events, TDC-fit is used. After the rings are re-fit, the total photo-electrons are apportioned to all of the rings. The momentum of a particle is determined from the total number of p.e.'s within a 70° half-angle of the cone relative to the track direction, with corrections for light attenuation and PMT angular acceptance. And the momentum from each ring is separated based on the expected p.e. distribution from each ring as a function of the opening angle.

Finally, the number of rings is corrected; Missfitted rings tend to have low momentum and overlap with the other energetic rings. MC simulation of atmospheric neutrino and the process of reduction and reconstruction are outlined well in [76].

Chapter 6

Search for $n - \bar{n}$ Oscillation

We should extract the candidates of $n - \bar{n}$ oscillation from the Super-K I data set of 24.5×10^{33} neutron-yr. For this work, additional criteria are applied to the remaining fully-contained (FC) data after passing through the reduction algorithm. Studying the FC atmospheric neutrino MC as a most significant source of background, we can estimate the upper limit of the number of $n - \bar{n}$ oscillation signal. Finally, the lower limit on neutron oscillation time is calculated with inclusion of systematic errors. In this thesis, 5,000 $n - \bar{n}$ events inside of fiducial volume (FV) and 100 years FC atmospheric neutrino MC are simulated for Super-K I data set.

6.1 Event Selection Criteria

Candidates of $n - \bar{n}$ oscillation are extracted based on (a) Number of rings, (b) Visible energy, (c) Total momentum and (d) Total invariant mass. The number of rings are understood particles produced by the interaction and visible energy is defined as the energy of an electromagnetic shower that gives a certain amount of Cherenkov light. The total momentum is defined as $P_{tot} = |\sum_i^{allrings} \vec{p}_i|$ where \vec{p}_i is reconstructed momentum vector of i -th ring and the total invariant mass is defined as $M_{tot} = \sqrt{E_{tot}^2 - P_{tot}^2}$ where total energy $E_{tot} = \sum_i^{allrings} |\vec{P}_i|$. Figure 6.1 is comparison of above 4 variables among the $n - \bar{n}$ MC, atmospheric neutrino MC and data after reduction and reconstruction processes in same way. To compare the plots, one addition is taken into account. Strong evidence has been presented that a ν_μ can oscillate to either a ν_τ or a sterile ν and this effect is observed only in charged current interaction. Therefore in the case of atmospheric neutrino MC, oscillation effect is applied at the $\sin^2 2\theta = 1$ and $\Delta m^2 = 0.0021$ as Eq. (6.1) since MC was made without considering the oscillation. As the plots show, the number of rings and visible energy are efficient variables to select the candidates. So, we can make first criterion to reject dominant background which comes from single ring events. The criterion rejects around 64% background events. Figure 6.2 is the visible energy distribution after rejecting the single ring events.

$$P(\nu_\mu \rightarrow \nu_\mu) = 1 - \sin^2 2\theta \sin^2 \left(1.27 \frac{\Delta m^2 L}{E_\nu} \right) \quad (6.1)$$

Our goal is to find the $n - \bar{n}$ oscillation events and calculate the oscillation time. If we don't find the events, we set the lower limit of oscillation time. The lifetime for neutron oscillations is estimated by

$$T_{n-\bar{n}} = \frac{\epsilon \times N \times T}{S}. \quad (6.2)$$

- ϵ : signal detection efficiency
- N : number of neutrons inside of fiducial volume
- T : detector livetime
- S : the upper limit on mean of number of signal at 90% CL

and the procedure of calculation is described in Chapter 6.3.

For optimization of selection criteria, signal significance is considered based on above calculation as follows ;

$$\frac{s}{\sqrt{b}} = \frac{\epsilon \times N \times T \times \Gamma}{\sqrt{b}} \quad (6.3)$$

where Γ is event rate and b is number of background candidates. Since $N \times T \times \Gamma$ is consistent,

$$\frac{s}{\sqrt{b}} \propto \frac{\epsilon}{\sqrt{b}} \quad (6.4)$$

ϵ/\sqrt{b} is used as a factor for criteria optimization. Optimal cut is found scanning the region which is low momentum and high invariant mass based on maximum value of ϵ/\sqrt{b} ;

- (a) Number of rings > 1
- (b) $700\text{MeV} < \text{Visible energy} < 1300\text{MeV}$
- (c) $0 \text{ MeV}/c < \text{Total momentum} < 450\text{MeV}/c$
- (d) $750\text{MeV}/c^2 < \text{Total invariant mass} < 1800\text{MeV}/c^2$

Criterion (a) and (b) rejected the 94% background events and saved 33.5% $n - \bar{n}$ MC and 6% signal. Figure 6.3 shows the total momentum and invariant mass distribution after passing through the criterion (a) and (b). Additional kinematical cuts, (c) and (d) made final sample which is inside of arrows in figure 6.4 for analysis.

6.2 Background

As mentioned above, the most significant source of background in $n - \bar{n}$ search comes from the atmospheric neutrino interactions as which on an average 8 FC events are detected per day during Super-K I full livetime. Therefore, investigation of the $n - \bar{n}$ mimic events is performed using the FC atmospheric neutrino MC. 521 FC atmospheric neutrino simulation events without inclusion of oscillation effect are alive after passing through the event selection criteria which was mentioned in previous section. The characteristic is listed up in Table 6.1 in detail. Electron neutrino and muon neutrino have almost same contribution to background but muon neutrino will be decreased by neutrino oscillation. And anti neutrino events are much

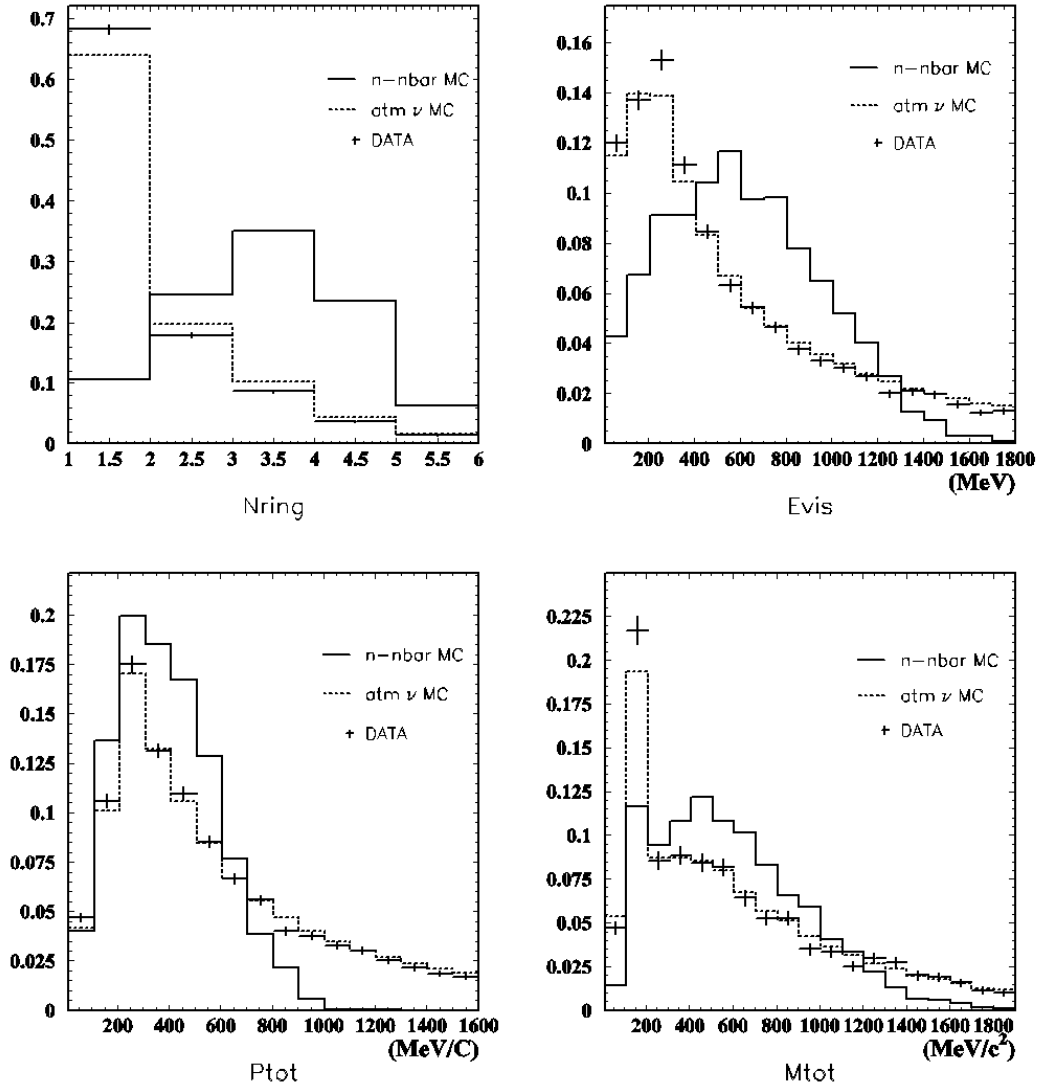


Figure 6.1: Basic plot comparisons : Each plot show Number of rings (Nring), Visible energy (Evis), Total momentum (Ptot) and Total invariant mass (Mtot). Vertical axes are normalized by the number of events and oscillation effect was applied in the case of atmospheric neutrino MC. A peak between 100 and 200 MeV/c² of Mtot distribution is caused by π^0 .

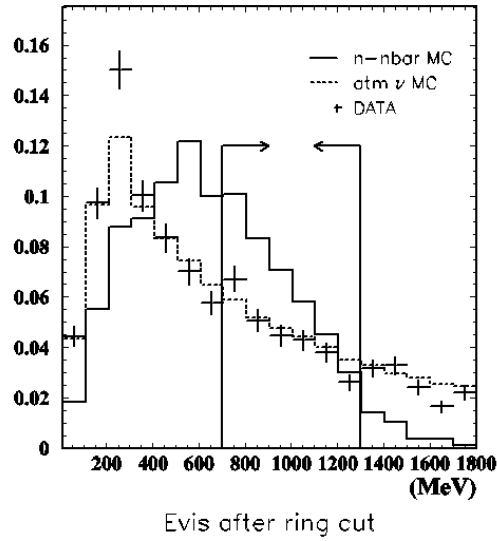


Figure 6.2: Visible energy distribution when the number of rings is greater than one. The arrows show the selection region of visible energy for this analysis.

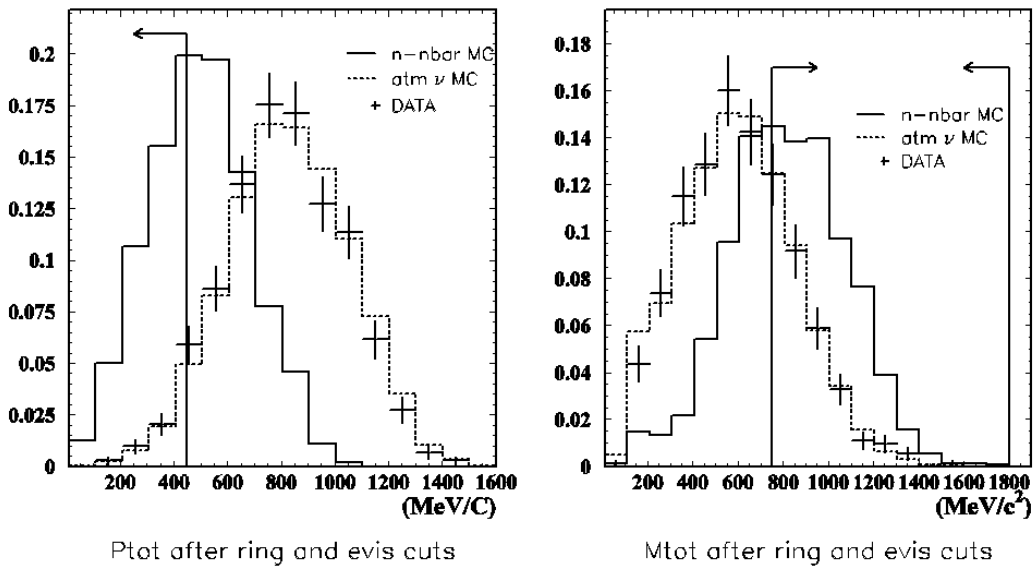


Figure 6.3: Total momentum and Invariant mass after passing through the selection criterion (a) and (b).

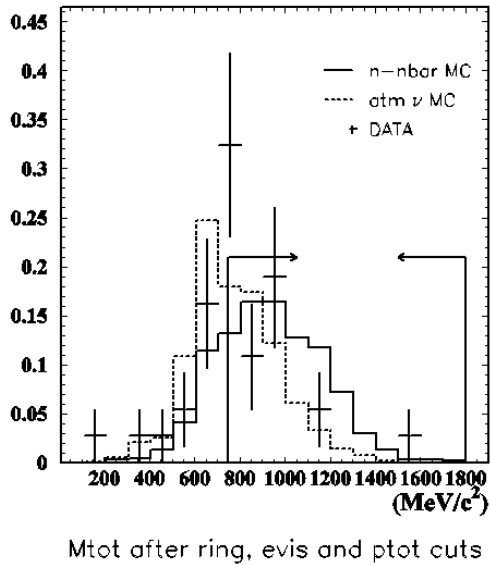


Figure 6.4: Invariant mass after passing through the selection criterion (a), (b) and (c).

less than neutrino events. Main contribution is single pion and multi pion production. The reason can be simply understood, produced pions and particles by neutrino interaction and secondaries make multi rings. Remarkable thing is, topologically even though charged current quasi elastic events should be separated from $n - \bar{n}$ events since they have larger momentum, they survived in analysis sample because energetic outgoing nucleon made hadron interactions. The neutral current elastic events are also survived in same way. Figure 6.5 shows the parent neutrino energy distribution for all of background events.

6.3 Results

Final detection efficiency of $n - \bar{n}$ events and the number of background and candidates after passing through above criteria are summarized in Table

| | ν_μ | $\bar{\nu}_\mu$ | ν_e | $\bar{\nu}_e$ |
|-----------------------|--------------|-----------------|--------------|---------------|
| CC quasi elastic | 11 (2.11%) | 0 | 7 (1.34%) | 0 |
| CC single π prod. | 50 (9.6%) | 10 (1.92%) | 47 (9.02%) | 7 (1.34%) |
| CC multi π prod. | 101 (19.38%) | 10 (1.92%) | 103 (19.77%) | 9 (1.73%) |
| CC K or η prod. | 6 (1.15%) | 6 (1.15%) | 8 (1.53%) | 1 (0.19%) |
| NC single π prod. | | 17 (3.26%) | | |
| NC multi π prod. | | 125 (23.99%) | | |
| NC K or η prod. | | 2 (0.38%) | | |
| NC elastic | | 1 (0.19%) | | |

Table 6.1: List of background events.

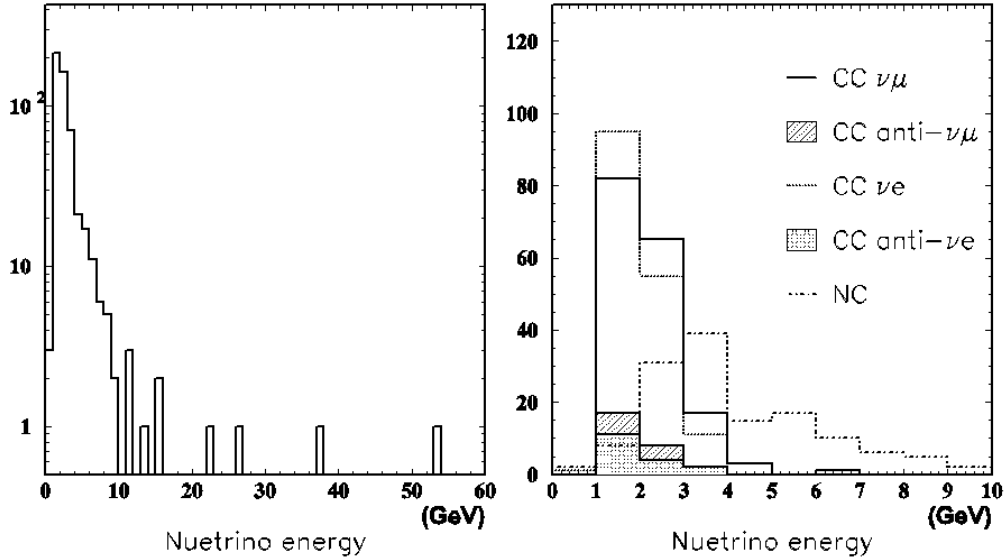


Figure 6.5: Parent neutrino energy of background events. Left figure shows about 521 background events in total and right figure shows in each interaction mode.

6.2. For this estimation, atmospheric neutrino MC considered the oscillation effect and overall normalization[76], a factor of 1.119, and is normalized by livetime. The detection efficiency is 10.4% and the candidates from Super-K I of 91.7kton-year exposure are 20 events in which 21 background events are allowed. Figure 6.6 shows final sample for analysis which is selected by kinematical cuts.

6.3.1 Simple Limit Calculation

When we observe N particles for a time T and find a nonzero number of events, n , with the detection efficiency, ϵ , the event rate, Γ is estimated by;

$$\Gamma = \frac{n}{NT\epsilon} \quad (6.5)$$

However, when n is zero, a rate can not be accurately calculated and n is no longer a good estimator of the true mean. So, instead, a limit on the event rate (oscillation rate in this thesis) at some confidence level is set.

Our result has 20 candidate events but also has background with almost same level. So, we interpret our result as lower limit of $n - \bar{n}$ oscillation

| Criterion | $n \rightarrow \bar{n}$ MC (%) | atm. ν MC (%) | DATA (%) |
|-----------------------------|--------------------------------|-------------------|-------------|
| Inside of F.V. | 5000 | 13028.9 | 12180 |
| Nring cut | 4275 (85.5) | 4676.7 (35.8) | 3865 (31.7) |
| Evis cut | 1673 (33.5) | 909.5 (7.0) | 731 (6.0) |
| P_{tot} and M_{tot} cut | 521 (10.4) | 21.6 (0.16) | 20 (0.16) |

Table 6.2: Number of events and detection efficiency after each criterion.

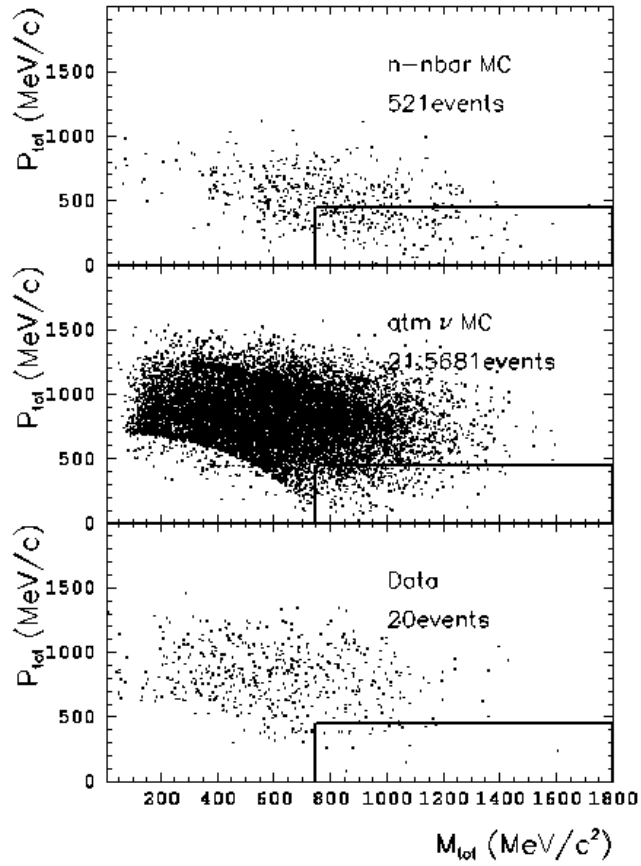


Figure 6.6: Total invariant mass versus total momentum. The events inside of right lower box in each scatter plot are final sample selected by kinematical cuts for $n - \bar{n}$ oscillation analysis. With 10.4% detection efficiency in which 521 events are detected among 5,000 $n - \bar{n}$ events, 20 candidates and 21 background events are observed.

time and the limit is calculated by Eq. (6.2) using the quantities in Table 6.2. In simple case, it is common to use the method of Poisson Process with Background[77]. However since this method does not take any uncertainties that we may have in the parameters to get the limit, the final limit will be estimated with other method considering the effect of systematic errors in last of this Chapter. Firstly, assuming that the systematic uncertainty is negligible and the number of background(μ_B) is known, the lower limit of oscillation time is calculated simply.

The upper limit on mean of the number of signal S in Eq. (6.2) can be defined using Poisson distribution[77]:

$$CL = 1 - \frac{e^{-\mu_B+S} \sum_{n=0}^{n_0} \frac{(\mu_B+S)^n}{n!}}{e^{-\mu_B} \sum_{n=0}^{n_0} \frac{(\mu_B)^n}{n!}} \quad (6.6)$$

where CL is a confidence level and n_0 is the number of observed candidates. Applying $n_0 = 20$ and $\mu_B = 21.6$, the upper limit S is calculated to be 7.95 at the 90% confidence level. Based on this S , the lower limit on the neutron oscillation time is calculated as:

$$T_{n-\bar{n}} = \frac{\epsilon \times v \times N_A \times \frac{8neutrons}{18g} \times T}{S} \quad (6.7)$$

For exposure, v is the fiducial volume of 22.5 kton, N_A is Avogadro's number and T is livetime of 4.07 years. ϵ is the efficiency to detect neutron oscillations, 10.4%. Therefore, the neutron oscillation time limit is calculated to be 3.2×10^{32} yr at the 90% confidence level for 24.5×10^{33} neutron-yr.

6.3.2 Limit for Free Neutrons

The lifetime of a neutron bound in a nucleus with A nucleons (T_A) is much larger than that of a free neutron (τ_{free}) due to the suppression of neutron oscillations by a potential barrier at the edge of the nuclear potential well.

As already mentioned, our search in this thesis is about intranuclear process. Limit can be converted to the limit for free neutron by theoretical nuclear suppression factor[12][13][14] with following relation.

$$T(intranuclear) = R \cdot \tau_{n\bar{n}}^2(free) \quad (6.8)$$

where R is dimensional "suppression factor" equal to $\sim 2 \cdot 10^{23} sec^{-1}$ for the most of nuclei. This can be understood from the following considerations simply.

The neutron bound in nucleus by energy $\Delta E(\sim 10MeV)$ is quasi-free for the time

$$\Delta t \sim \frac{1}{\Delta E} \sim 10^{-22} sec \quad (6.9)$$

Probability of $n - \bar{n}$ oscillation during the time Δt is

$$P = \left(\frac{\Delta t}{\tau_{n\bar{n}}}\right)^2 \quad (6.10)$$

and above condition occurs per second.

$$P = \frac{1}{T(\text{intranuclear})} = \left(\frac{\Delta t}{\tau_{n\bar{n}}}\right)^2 \frac{1}{\Delta t} = \frac{\Delta t}{(\tau_{n\bar{n}})^2} \quad (6.11)$$

Intranuclear process are heavily suppressed by R .

$$T(\text{intranuclear}) = R \cdot (\tau_{n\bar{n}}(\text{free}))^2 \quad (6.12)$$

$$R \sim \frac{1}{\Delta t} \sim 10^{22} s^{-1} \quad (6.13)$$

We call R as nuclear suppression factor. Theoretical progresses on R are described on [12][13][14] and R of ^{16}O is suggested $(0.46 \sim 1.93) \times 10^{-23}$ by Dover et al., $(1.7 \sim 2.6) \times 10^{-23}$ by Alberico and $(0.6 \sim 3.6) \times 10^{-23}$ by Hüfner and Kopeliovich. The most conservative limit is $R = 3.6 \times 10^{23} s^{-1}$ in most recent theoretical treatment of [14].

Finally, oscillation time limit on bound neutron in previous section can be translated to $1.67 \times 10^8 s$ on free neutron by most conservative limit of nuclear suppression factor.

6.4 Systematic Errors

We simulated $n - \bar{n}$ oscillation and background for $n - \bar{n}$ search and got the lower limit on neutron oscillation time. However, the limit is affected by uncertainties in detection efficiency and background due to imperfection of simulation and measurement. In this section, I estimate the systematic errors in our $n - \bar{n}$ analysis.

6.4.1 Uncertainties in Efficiency and Exposure

Incompleteness and model dependence in simulation of $n - \bar{n}$ oscillation lead to systematic errors. By estimating the contribution to detection efficiency and exposure from each source of uncertainties, systematic errors in analysis are obtained. The sources of uncertainties are listed up below;

- Detection efficiency
 - Fermi momentum
 - Annihilation branching ratio
 - Nuclear effect
 - Un-uniformity of detector gain
 - Energy scale
 - Ring counting
- Exposure
 - Detector livetime
 - Fiducial volume

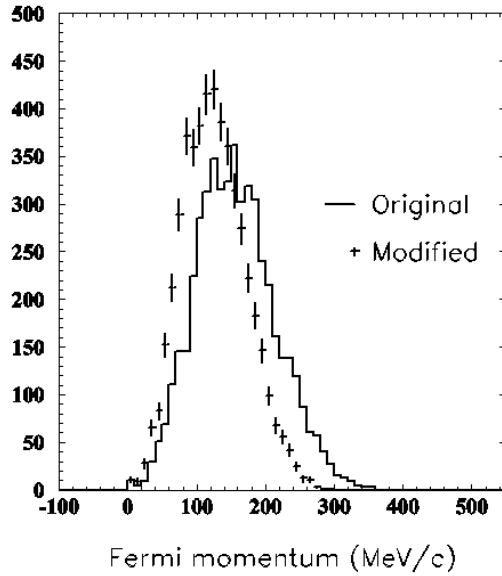


Figure 6.7: Fermi momentum distribution.

The uncertainty is caused by imperfect knowledge of $n - \bar{n}$ oscillation kinematics. First, I estimated how much fermi momentums of anti-neutron and nucleon, which participate in annihilation process, affect to detection efficiency. Figure 6.7 shows fermi momentum of anti-neutron which was transited from neutron. Changing the fermi momentum by 20%, the contribution to detection efficiency is estimated to be 4.2%. And annihilation branching ratio can be source of uncertainty. Table 4.1 and 4.2 in Chapter 4 show the annihilation branching ratios which are used in this thesis and other experiments. For uncertainty estimation, we generated $n - \bar{n}$ oscillation MC with other branching ratios, Baltay(1966) for $\bar{n} - n$ annihilation and Bettini(1967) for $\bar{n} - p$ annihilation, and got the change of detection efficiency by 5.2%. Nuclear effect in pionic phase after annihilation is considered as a main source of uncertainty in efficiency. The errors of cross section are taken from the figure 4.2. Increasing the probability by 20% of elastic, 30% of charge exchange, 25% of absorption and 30% π production, the uncertainty in efficiency is estimated to be 12.5%. And to check model dependency of nuclear effect, nuclear propagation program "eftrace" for nucleon decay study in Super-K analysis is called in $n - \bar{n}$ simulation process instead of "partnuc" which is $n - \bar{n}$ own nuclear propagation program. Obtaining the small uncertainty of 1.7%, the reasonable consistency of our simulation is checked with other Model.

And event selection and reconstruction process include possible sources of uncertainties. For "neutrino" oscillation study[76] in Super-K, the difference of energy scale between upward-going and downward-going events was measured using decay electrons from cosmic ray stopping muons. The up/down asymmetry of energy scale was estimated to be 0.6% and this non-uniformity of energy scale can affect momentum measurement which is one of criteria for $n - \bar{n}$ search. Therefore by changing the momentum cut by $\pm 1.2\%$, we obtained 4% uncertainty in efficiency. In neutrino oscillation

study in Super-K, the uncertainty of energy scale for fully-contained events was also estimated to be 2%. Based on this report, visible energy cut is changed by 2.5% and the contribution to efficiency is estimated to be 1.7%. And for final consideration, we tested the possibility of uncertainty from ring counting and I'd like to describe procedure of this study in detail below.

Ring candidates are tested by a likelihood method as explained in Chapter 5.2.2. If there is systematic difference of likelihood between data and MC due to some reason (water transparency, incomplete understanding of the geometry etc.), it can be source of uncertainty. To investigate the systematic difference of likelihood, atmospheric neutrino data and MC between 8,000 p.e. and 13,000 p.e. are selected as the sample. Comparing the likelihood distribution between data and MC with some offset, we find the minimum χ^2 defined as $(data - \alpha MC)^2 / \sigma^2$. Figure 6.8 shows the likelihood comparison and χ^2 result for 1ring/2more ring separation. The center values of parabola fitted around the minimum χ^2 region are taken as systematic errors of likelihood function. This process is also applied for higher ring separations and Figure 6.9 shows the results. The quantities of the errors estimated above are summarized in Table 6.3. Finally to estimate the uncertainty caused by ring counting in efficiency of $n - \bar{n}$ search, ring reconstruction process is newly applied to $n - \bar{n}$ MC with new likelihood threshold changed by the error estimated in each ring separation. Changing the threshold of likelihood, the number of $n - \bar{n}$ events passing through selection criteria is changed by 0.6%.

| Separation | minimum $\chi^2 \pm 1\sigma$ |
|------------------|------------------------------|
| 1ring/2more ring | - 0.733 \pm 0.137 |
| 2ring/3more ring | - 0.623 \pm 0.142 |
| 3ring/4more ring | - 0.804 \pm 0.297 |
| 4ring/5more ring | + 0.198 \pm 0.480 |

Table 6.3: Fitted minimum χ^2 of likelihood function for ring counting. We assume these difference from same reason and change the threshold coherently.

Oscillation time limit is also directly affected by exposure. So, the uncertainties in the exposure are estimated. The livetime is calculated from the 48bit clock counter information recorded in TRG module. The uncertainty of the observed livetime is estimated by comparing the clock counter with another clock counter to be $< 0.1\%$. Lastly, uncertainty of fiducial volume is estimated by comparing the number of events inside and outside of fiducial volume in the case of FC data and MC as follows ;

$$\frac{DATA_{in}/DATA_{out}}{MC_{in}/MC_{out}} = 0.99 \pm 0.03 \quad (6.14)$$

Above estimation is done using the events of which the number of ring is over two and visible energy is over 30GeV. Uncertainty of fiducial volume is estimated to be 3.2%.

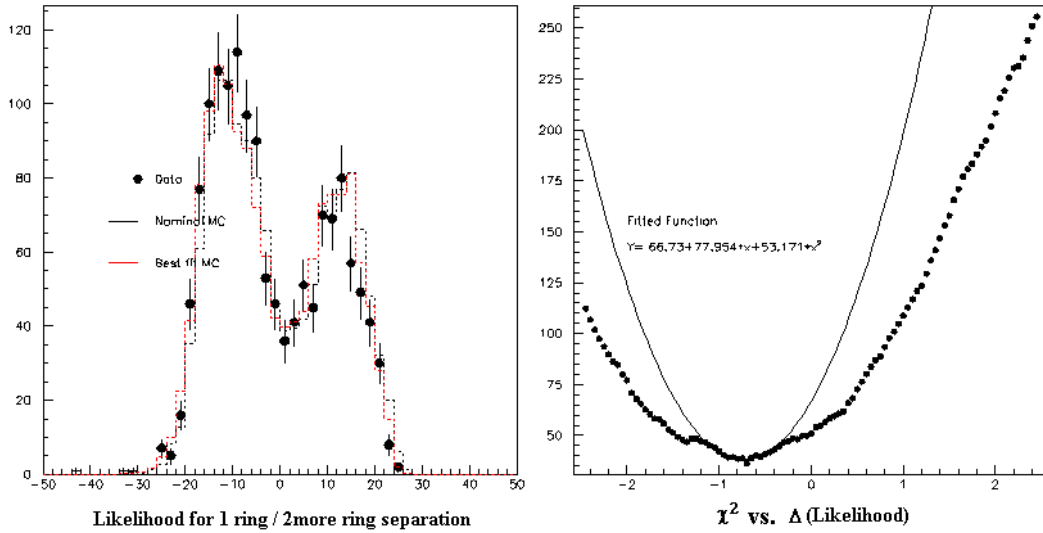


Figure 6.8: Likelihood distribution and minimum χ^2 .

All of uncertainties in efficiency and exposure are summarized in Table 6.4 and systematic uncertainty in total is estimated to be less than 15.2%.

| | Uncertainty (%) |
|--|-----------------|
| Detection Efficiency | 14.9 |
| fermi momentum | 4.2 |
| annihilation branching ratio | 5.2 |
| un-uniformity of detector gain | 4.0 |
| energy scale | 1.7 |
| ring counting | 0.6 |
| nuclear propagation (model dependence) | 1.7 |
| nuclear propagation (cross section) | 12.5 |
| Exposure | < 3.2 |
| detector livetime | <0.1 |
| fiducial volume | 3.2 |
| Total | <15.2 |

Table 6.4: Systematic uncertainties in efficiency and exposure.

6.4.2 Uncertainties in Background

The uncertainties in background also affect to the lower limit on $n - \bar{n}$ oscillation time. Neutrino flux and interaction can be sources of uncertainties since we suppose the fully-contained atmospheric neutrino is main background. And uncertainties related to events selection and reconstruction are also considered, such as un-uniformity, energy scale and ring counting in common with the estimation of uncertainty in efficiency.

The detail descriptions of the uncertainties for the atmospheric neutrino flux and interaction in MC simulation were presented in Chapter 4.2 and 4.3.

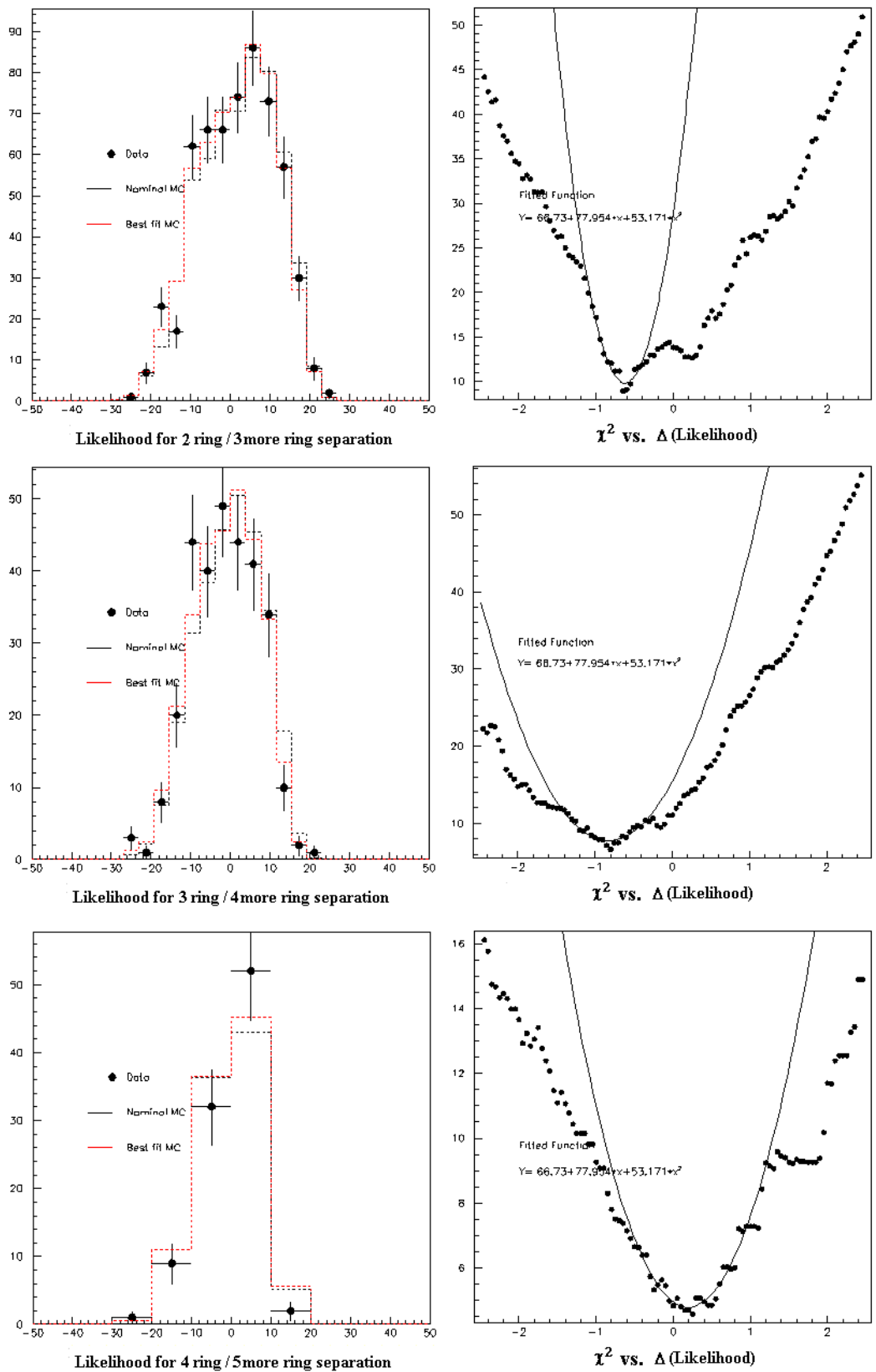


Figure 6.9: Likelihood distribution and minimum χ^2 . From the top, it is for 2ring/3more ring separation, 3ring/4more ring separation and 4ring/5more ring separation.

By changing the neutrino flux and interaction by the errors, uncertainties in background rate are estimated and summarized in Table 6.5. Uncertainties by un-uniformity, energy scale and ring-counting are estimated in same way of estimation in efficiency. Changing the boundary values of selection criteria for visible energy and total momentum changes the number of background by 9% and 12% respectively. And to estimate uncertainty by ring-counting, ring reconstruction process which has the change of likelihood threshold by the errors is applied to FC atmospheric neutrino MC and contribution to background rate is estimated to be 4.3%. The total systematic uncertainty in background rate is estimated to be 32.1%.

| | Err.(%) | Uncert.(%) |
|--|-----------------------------------|------------|
| Neutrino Flux | | 21.5 |
| flux absolute normalization | 20 | 20 |
| flavor ratios ($E_\nu < 5\text{GeV}, > 5\text{GeV}$) | 3, 3-10, | -, 0.1 |
| $\bar{\nu}_e/\nu_e$ ratio ($E_\nu < 10\text{GeV}, > 10\text{GeV}$) | 5, 5-10 | 0.9, - |
| $\bar{\nu}_\mu/\nu_\mu$ ratio ($E_\nu < 10\text{GeV}, > 10\text{GeV}$) | 5, 5-25 | 0.8, - |
| up/down ratio | 0.4-2.1 | - |
| horizontal/vertical ratio | 0.3-2.8(3D calc.) | - |
| K/π ratio | 20 | 5.2 |
| energy spectrum | 0.05 for $E_p > 100\text{GeV}$ | 5.8 |
| Neutrino Cross Section | | 18 |
| M_A in quasi-elastic and single- π | 10 | 4.4 |
| QE scattering (model dependence) | 1σ =Fermi-gas vs. Oset | - |
| QE scattering (cross section) | 10 | 0.4 |
| single- π production (cross section) | 10 | 2.8 |
| multi- π production (model dependence) | 1σ =w/ vs. w/o Bodek | 15.5 |
| multi- π production (cross section) | 5 | 3.4 |
| coherent π production (cross section) | 30 | 0.1 |
| NC/CC ratio | 20 | 6.2 |
| nuclear effect in ^{16}O (mean free path) | 30 | 2.7 |
| Un-uniformity of Detector Gain | | 9.0 |
| Energy Scale | | 12.0 |
| Ring Counting | | 4.3 |
| Total | | 32.1 |

Table 6.5: Systematic uncertainties in background rate.

6.5 Final Limit Calculation

In section 6.3, simple limit calculation using Poisson distribution is performed assuming the systematic uncertainties to be negligible. In this section, all of systematic uncertainties are included in the limit calculation by employing a Bayesian method[78][79].

6.5.1 Description of Method

The expected mean number of candidates, μ , in our data sample is

$$\mu = \Gamma\lambda\epsilon + b \quad (6.15)$$

where Γ is the true event rate ($n - \bar{n}$ oscillation rate in this analysis), $\lambda = NT$ is the true exposure, ϵ is the true efficiency to detect oscillation events and b is the true mean number of background events. In the counting experiments, the probability to detect n events follows the Poisson distribution with Poisson parameter μ .

$$P(n|\Gamma\lambda\epsilon b) = \frac{e^{-(\Gamma\lambda\epsilon+b)}(\Gamma\lambda\epsilon + b)^n}{n!} \quad (6.16)$$

$P(A|B)$ represents the probability of proposition A, given that proposition B is true.

Applying Bayes' theorem allows us to write

$$P(\Gamma\lambda\epsilon b|n)P(n) = P(n|\Gamma\lambda\epsilon b)P(\Gamma\lambda\epsilon b). \quad (6.17)$$

Because quantities $\Gamma, \lambda, \epsilon, b$ are independent, $P(\Gamma\lambda\epsilon b)$ can be disintegrated.

$$P(\Gamma\lambda\epsilon b) = P(\Gamma)P(\lambda)P(\epsilon)P(b) \quad (6.18)$$

The quantity in which we are interested, probability density function of Γ can be obtained by

$$P(\Gamma|n) = \int \int \int P(\Gamma\lambda\epsilon b|n)d\lambda d\epsilon db. \quad (6.19)$$

By combining above four equations, we obtain

$$P(\Gamma|n) = A \int \int \int \frac{e^{-(\Gamma\lambda\epsilon+b)}(\Gamma\lambda\epsilon + b)^n}{n!} P(\Gamma)P(\lambda)P(\epsilon)P(b)d\lambda d\epsilon db. \quad (6.20)$$

Above normalization factor A is resolved by demanding

$$\int_0^\infty P(\Gamma|n)d\Gamma = 1. \quad (6.21)$$

$P(\Gamma), P(\lambda), P(\epsilon), P(b)$ in Eq. (6.20) are prior probability density functions (priors) and they enable us to include systematic uncertainties in the limit calculation. Finally, we can calculate the upper limit of the event rate Γ^{limit} by

$$CL = \int_0^{\Gamma^{limit}} P(\Gamma|n)d\Gamma. \quad (6.22)$$

In this thesis, the limit is calculated at the 90% CL and the lifetime limit (oscillation time limit in this analysis) is the inverse of Γ^{limit} .

6.5.2 Priors

There are two classes of priors in this method. One contains Γ , the other contains ϵ, λ and b . In the former case, Γ is the parameter we wish to estimate with the experiment and in the latter, the parameters are not directly interesting and are marginalized out of the final result appearing in calculation process. Each prior is discussed below.

The prior for the event rate $P(\Gamma)$ is taken to be uniform. This corresponds to the uniform prior implicitly used in simple Poisson limits[77].

$$P(\Gamma) \propto \begin{cases} 1 & \Gamma > 0 \\ 0 & \textit{otherwise} \end{cases} \quad (6.23)$$

The priors for the exposure $P(\lambda)$ and detection efficiency $P(\epsilon)$ are taken as Gaussian distributions, truncated to disallow unphysical regions.

$$P(\lambda) \propto \begin{cases} e^{-(\lambda-\lambda_0)^2/2\sigma_\lambda^2} & \lambda > 0 \\ 0 & \textit{otherwise} \end{cases} \quad (6.24)$$

$$P(\epsilon) \propto \begin{cases} e^{-(\epsilon-\epsilon_0)^2/2\sigma_\epsilon^2} & 0 < \epsilon < 1 \\ 0 & \textit{otherwise} \end{cases} \quad (6.25)$$

where λ_0 and ϵ_0 are estimated exposure and efficiency. The values of σ_λ and σ_ϵ are taken from the Table 6.4 in the previous section.

The background prior $P(b)$ is taken to be a convolution of Poisson and Gaussian distributions in order to account for both the statistical uncertainty of a finite background MC sample size and the systematic uncertainty in the background MC sample.

$$P(b) \propto \int_0^\infty \frac{e^{-b^{MC}} (b^{MC})^{n_b}}{n_b!} e^{-\frac{(bC-b^{MC})^2}{2\sigma_b^2}} db^{MC} \quad (6.26)$$

where

- n_b : MC events passing through $n - \bar{n}$ oscillation criteria.
- b^{MC} : true mean MC events passing through $n - \bar{n}$ oscillation criteria.
- C : MC oversampling factor.
- σ_b : uncertainty due to neutrino fluxed and cross sections etc.

6.5.3 Results

The lower limit on $n - \bar{n}$ oscillation time is obtained by integrating the parameter in Eq. (6.20) and (6.22). To perform this, GNU Science Library which is available in [80] is used for this thesis. The lower limit on $n - \bar{n}$ oscillation time of bound neutrons is determined at the 90% *CL*,

$$T_{n-\bar{n}} > 1.78 \times 10^{32} \textit{yr} \quad (6.27)$$

incorporating most major sources of experimental uncertainties. And assuming the suppression factor in ^{16}O is $3.6 \times 10^{23} \textit{s}^{-1}$, the corresponding limit of free neutrons at the 90% *CL* is

$$\tau_{n-\bar{n}} > 1.25 \times 10^8 \textit{s}. \quad (6.28)$$

Chapter 7

Conclusion

A search for neutron-antineutron oscillation which is a process of $|\Delta B| = 2$ predicted by L-R symmetric gauge theories was undertaken using the 24.5×10^{33} neutron-yr exposure of the full Super-K I data set. In this thesis, most major sources of experimental uncertainties were incorporated. The uncertainty in detection efficiency was estimated to be 15.2% from 9 sources of systematic errors and in background was estimated to be 32.1% from 20 sources of errors.

A lower limit on oscillation time for neutrons bound in ^{16}O was determined to be 3.20×10^{32} yr at the 90% *CL* without inclusion of the effect of the systematic uncertainties and this limit is better than the previous best limit of 7.2×10^{31} yr in Soudan 2 by a factor of about 4.5. Above lower limit is reduced when the systematic uncertainties are included;

$$T_{n-\bar{n}} > 1.78 \times 10^{32} \text{ yr}$$

at the 90% *CL*. And the corresponding limit for free neutrons has been calculated to be

$$\tau_{n-\bar{n}} > 1.25 \times 10^8 \text{ s}$$

using a suppression factor of $3.6 \times 10^{23} \text{ s}^{-1}$ which is a relatively large compared to previous theoretical estimation for ^{16}O .

A Comparison of Super-K I limits with previous neutron oscillation limits in other nucleon decay experiments is given in Table 7.1. The result in Super-K I has relatively many candidates with small detection efficiency. Thus, we hope to have a better limit in near future with improved event selection criteria that will increase signal detection efficiency and reduce the number of background events per unit exposure combining the Super-K II data set. This means our new selection criteria will improve the ability to identify the Cherenkov rings from the annihilation products.

The L-R symmetric based models that allow neutron oscillations include an explanation for the neutrino mass and the origin of masses for quarks as well as leptons. Therefore, search for neutron oscillations may also give us indirect informations on those.

| Experiment | Exposure[λ] ($10^{32} \text{neutron} - \text{yr}$) | Efficiency[ϵ] (%) | Candidate (<i>events</i>) | Signal limit[s] (<i>events</i>) |
|------------|---|---------------------------------|--------------------------------|--------------------------------------|
| Super-K I | 245.5 | 10.4 | 20 | 8.0 |
| Soudan 2 | 21.9 | 18.0 | 5 | 5.5 |
| Frejus | 5.0 | 30.0 | 0 | 2.3 |
| Kamiokande | 3.0 | 33.0 | 0 | 2.3 |
| IMB | 3.2 | 11.9 | 0 | 2.3 |

| Experiment | Limit for bound neutrons[T] (10^{32}yr) | | Limit for free neutrons[τ] (10^8s) | |
|-----------------------|--|------|--|------|
| (syst. uncertainties) | w/o | w/ | w/o | w/ |
| Super-K I | 3.20 | 1.78 | 1.67 | 1.25 |
| Soudan 2 | 0.72 | 0.47 | 1.3 | 0.61 |
| Frejus | 0.65 | - | 1.2 | - |
| Kamiokande | 0.43 | - | 1.2 | - |
| IMB | 0.24 | - | 1.1 | - |

Table 7.1: The lower limits on $n-\bar{n}$ oscillation time at the 90% CL in nucleon decay experiments. Oscillation time limit is calculated by $T = \epsilon \cdot \lambda/s$. The limits for free neutrons are deduced from the limits for bound neutrons by the suppression factor, $T = R \cdot \tau^2$, and Super-K I limit used a suppression factor of $3.6 \times 10^{23} \text{s}^{-1}$.

Bibliography

- [1] Sakharov A.D., JETP lett. 5, pp 24-27 (1967); Sov. Phys. Usp. 34, pp. 392-393 (1991).
- [2] Kuzmin V.A., JETP Lett. 12, p.228 (1970); ZhETF Pis. Red. 12, No. 6, p.335 (1970); Izvestiya AN SSSR ser. Phys. 35, 2088 (1971).
- [3] Goldhaber M., Search for Nucleon Instability (Origin and History), in the Proceedings of International Workshop on Future Prospects of Baryon Instability Search in p -Decay and $n \rightarrow \bar{n}$ Oscillation Experiments, Oak Ridge, pp.1-6 (1996).
- [4] Pati J. and Salam A., Phys. Rev. D8, 1240 (1973); Phys. Rev. Lett 31, pp. 661-664 (1973); Phys. Rev. D10, pp. 275-289 (1974).
- [5] Georgi H. and Glashow S.L., Phys. Rev. Lett. 32, pp. 438-441 (1974).
- [6] 't Hooft G., Phys. Rev. Lett. 37, 8-11 (1976); Phys. Rev. D14, pp. 3432-3450 (1976).
- [7] H. Murayama and A. Pierce, Phys. Rev. D65, 055009-1 (2002).
- [8] K. Kobayashi et al., hep-ex/0502026 (2006).
- [9] Z. Chacko and R.N. Mohapatra, Phys. Rev. D 59, 055004 (1999); K.S. Babu and R.N. Mohapatra, Phys. Lett. B 518, 269 (2001).
- [10] M. Baldo-Ceolin et al., Z. Phys. C63, 409-416 (1994), R. N. Mohapatra, in the Proceedings of the International Workshop on the Future Prospects of Baryon Instability Search in Proton-Decay and Neutron-Antineutron Oscillation Experiments, Oak Ridge, March 28-30, 1996; also hep-ph/9604414.
- [11] Y. Kamyshev, Nucl. Phys. 52A, 263-268 (1997), hep-ex/0211006 (2002).
- [12] C. B. Dover et al., Phys. Rev. D27, 1090-1100 (1983).
- [13] W. M. Alberico, $n - \bar{n}$ Suppression in Intranuclear Transitions (review) and references therein, in the Proceedings of the International Workshop on the Future Prospects of Baryon Instability Search in Proton-Decay and $n \rightarrow \bar{n}$ Oscillation Experiments, Oak Ridge, March 28-30, 1996; J. Jufner and B. Z. Kopeliovich, Mod. Phys. Lett. A13, 2385-2392 (1998), hep-ph/9807210 (1998).

- [14] J. Hufner and B. Z. Kopeliovich, *Mod. Phys. Lett.* A13, 2385 (1998).
- [15] T. W. Jones et al., IMB collaboration, *Phys. Rev. Lett.* 52, 720-723 (1984).
- [16] M. Takita et al., Kamiokande experiment, *Phys. Rev.* D34, 902-904 (1986).
- [17] Ch. Berger et al., Fréjus Collaboration, *Phys. Lett.* 240, 237-242 (1990).
- [18] J. Chung et al., hep-ex/0205093 (2006).
- [19] J. Formaggio, talk at the International Workshop on Neutron-Antineutron Transition Search with Ultracold Neutrons, 13-14 September 2002, Indiana University, Bloomington.
- [20] R. E. Marshak and R. N. Mohapatra, *Phys. Lett.* 91B, 222 (1980).
- [21] R. N. Mohapatra and R. E. Marshak, *Phys. Rev. Lett.* 44, 1316 (1980).
- [22] P. Langacker, in *Proceedings of the Twelfth International Symposium on Lepton and Photon Interactions at High Energies*, Kyoto, 1985, edited by M. Konuma and K. Takahashi, p.186 (Nahissha Printing Co., Kyoto, Japan, 1986).
- [23] K. Arisaka et al., *J. Phys. Sco. Jpn.* 54, 3213 (1985).
- [24] H. S. Park et al., *Phys. Rev. Lett.* 54, 22 (1985); G. Blewitt et al., *ibid.* 55, 2114 (1985).
- [25] D. Chang et al., *Phys. Rev.* D31, 1718 (1985); J. Gipson et al., *Phys. Rev.* D31, 1705 (1985).
- [26] F. Buccella et al., *Phys. Lett.* B233, 178 (1989); J. Gipson et al., *Phys. Rev.* D31, 1705 (1985).
- [27] T. Yanagida, *Proc. of the Workshop on the Unified theory and Baryon Number in the Universe*, KEK report 79-18, 95 (1979).
- [28] N. T. Shaban and W. J. Stirling, *Phys. Lett.* B291, 281 (1992).
- [29] D. Lee, R. N. Mohapatra, M. K. Parida and M. Rani, *Phys. Rev.* D51, 229 (1995).
- [30] J. Pasupathy, *Phys. Lett.* 114B, 172 (1982); S. P. Misra and U. Sarkar, *Phys. Rev.* D28, 249 (1983); S. Rao and R. Shrock, *Phys. Lett.* 116B, 238 (1982).
- [31] R. N. Mohapatra and R. E. Marshak, *Phys. Lett.* 94B, 183 (1980).
- [32] Super-Kamiokande Detector, *Nucl. Instrum. Meth.* A501, 418-462 (2003).
- [33] I. Frank and I. Tamm, *C. R. Acad. Sci. USSR* 14, 109 (1937).
- [34] R. Claus et al., *Nucl. Inst. and Meth.* A 261, 540 (1987).

- [35] Surface Optics Corp, San Diego, Report No. SOC-R950-001-0195 (1995).
- [36] R. Armenteros and B. French, in High Energy Physics, edited by E. H. S. Burhop, Vol. 4, p.237 (Academic, New York, 1969).
- [37] P. Pavlopoulos et al., in Nucleon-Nucleon Interactions-1977, edited by H. Fearing, D. Measday, and A. Strathdee, AIP Conference Proceedings No. 41, p. 340, See in particular the table on page 347 (American Institute of Physics, New York, 1978).
- [38] A. Backenstoss et al., CERN Report No. CERN-EP/83-58 (1983).
- [39] M. Sandel et al., Phys. Rev. C20, 744 (1979).
- [40] C. B. Dover, A. Gal, and F. M. Richard, Phys. Rev. D 27, 1090 (1983).
- [41] R. Hofstadter, Rev. Mod. Phys. 28, 214 (1956).
- [42] D. Ashery, Nucl. Phys. A354, 555 (1981).
- [43] G. Battistoni, A. Ferrari, T. Montaruli, and P. R. Sala (2003), hep-ph/0305208.
- [44] M. Honda, T. Kajita, K. Kasahara, and S. Midorikawa, Phys. Rev. D70, 043008 (2004), astro-ph/0404457.
- [45] G. D. Barr, T. K. Gaisser, P. Lipari, S. Robbins, and T. Stanev, Phys. Rev. D70, 023006 (2004), (Also, private communication with the authors. A slightly different flux from the one discussed in the paper is used in the present analysis.), astro-ph/0403630.
- [46] Y. Shikaze et al., Proc. of the 28th International Cosmic Ray Conferences (ICRC2003), Vol 7, p.4027 (2003).
- [47] <http://ulysses.sr.unh.edu/NeutronMonitor/>.
- [48] J. Alcaraz et al. (AMS), Phys. Lett. B490, 27 (2000).
- [49] T. Sanuki et al., Astrophys. J. 545, 1135 (2000), astro-ph/0002481.
- [50] P. Lipari, Nucl. Phys. B (Proc. Suppl.) 81, 159 (2001).
- [51] M. Nakahata et al., of Phys. Soc. Japan. 55, 3786 (1986).
- [52] C. H. Llewellyn Smith, Phys. Rept. 3, 261 (1972).
- [53] R. A. Smith and E. J. Moniz, Nucl. Phys. B43, 605 (1972).
- [54] D. Rein and L. M. Sehgal, Ann. Phys. 133, 79 (1981).
- [55] D. Rein, Z. Phys. C35, 43 (1987).
- [56] T. Kitagaki et al., Phys. Rev. D34, 2554 (1986).
- [57] S. K. Singh, M. J. Vicente-Vacas, and E. Oset, Phys. Lett. B416, 23 (1998).

- [58] M. H. Ahn et al. (K2K), Phys. Rev. Lett. 90, 041801 (2003), hep-ex/0212007.
- [59] D. Rein and L. M. Sehgal, Nucl. Phys. B223, 29 (1983).
- [60] M. Gluck, E. Reya, and A. Vogt, Z. Phys. C67, 433 (1995).
- [61] M. Nakahata et al. (KAMIOKANDE), J. Phys. Soc. Jap. 55, 0 3786 (1986).
- [62] T. Sjostrand, Comput. Phys. Commun. 82, 74 (1994).
- [63] R. Woods and D. Saxon, Phys. Rev. 95, 577 (1954).
- [64] L. L. Salcedo, E. Oset, M. J. Vicente-vacas, and C. Garcia-Recio, Nucl. Phys. A484, 557 (1988).
- [65] G. Rowe, M. Salomon, and R. H. Landau, Phys. Rev. C18, 584 (1978).
- [66] D. Ashery et al., Phys. Rev. C23, 2173 (1981).
- [67] GEANT, CERN Program Library Long Writeup W5013 (1994).
- [68] C. Zeitnitz and T.A. Gabriel, Nucl. Inst. and Meth. A349, 106 (1994).
- [69] M. Nakahata et al., J. Phys. Soc. Jpn. 55, 3786 (1986).
- [70] E. Bracci et al., CERN/HERA 72-1 (1972).
- [71] A.S. Carrl et al., Phys. Rev. C 14, 635 (1976).
- [72] M. Shiozawa, Ph.D. Thesis, University of Tokyo (1999).
- [73] E.Davis, Machine Vision : Theory, Algorithms, Practicalities (Academic Press, San Diego, 1997).
- [74] M. Ishitsuka, Ph.D. Thesis, University of Tokyo (2004).
- [75] S.Kasuga et al., Phys. Lett. B374, 238 (1996).
- [76] Y.Asie et al. (Super-Kamiokande), Phys. Rev. D 71, 112005 (2005), hep-ex/0501064.
- [77] R. M. Barnett et al., Phys. Rev. D54, 1 (1996).
- [78] T.J. Loredo, in Maximum Entropy and Bayesian Methods, edited by P.F. Foug 'ere(Kluwer Academic, Dordrecht, The Netherlands, 1990).
- [79] B. Viren, Super-Kamiokande Report No. 98-3, (1998).
- [80] <http://www.gnu.org/software/gsl/>

Acknowledgement

I'd like to express my deep appreciation to people who made many efforts until this dissertation came out although this writing might not be enough to express that.

To my advisor, Prof. Jae-Yool Kim, I'd like to thank firstly. He gave me nice chance and nice environment to keep the High Energy Physics Experiment continuously. And I would also like to give my thanks to Prof. In-Taek Lim, he cared me like as daughter encouraging me every time. And I thank to every Korean members in Super-Kamiokande beginning with Prof. Soo-Bong Kim. I was happy to work with them.

Until the analysis result came out in this dissertation, several people actually made many efforts. I greatly thank to people in California State University of Dominguez Hills and Kameda san. Especially, Prof. Ganezer as a beginner for this study in Super-Kamiokande, introduced and taught me many things about physics topic in this dissertation and I really thank to him for much kindness so far. Dr. Brandon Hartfiel in CSUDH and Kameda san in ICRR contributed largely to finalizing this analysis during last 1 year. Brandon did detail check of our Monte Carlo and Kameda san did uncertainty estimation of ring counting and Background search. Prof. Ganezer, Brandon and Kameda san helped me even to revise my dissertation. I deeply thank to them. And I thank to Prof. Jim Hill and Dr. William E. Keig for their constant concern with this analysis.

All of members in analysis group for Atmospheric neutrino and Proton decay, have given us constant concern and comments. Especially, I'd like to express great appreciation to Kajita san. We could finalize this analysis due to his careful concern and detail comments. And I bothered so much Shiozawa san in ICRR and Kobayashi san in Stony Brook University and learned many analysis technics.

I'm obliged to all of staff beginning with Suzuki san and Nakahata san in ICRR and Kamioka Observatory. I could enjoy staying in Japan for a long time due to their consideration. While I worked in calibration group, I was taught many things including electronics by experts beginning with Moriyama san and the staff were of much help. I really appreciate all of staff and students in Kamioka again.

I can not except all of Professors who taught and support me in Department of Physics and Physics Education in Chonnam National University from this acknowledgement and I'd like to express appreciation to them. I also thank to students and seniors in Laboratory for High Energy Physics. Especially I deeply thank to Kyung-Ju Ma who is my senior and was friend during last 1 year in which we prepared for graduating together.

I know I can be here due to my parents' pray. They gave best support to study, so far. I'd like to give my best thank to my family including him who is my best friend in my whole life, constant supporter of me and my husband. I also deeply thank to family in law for their consideration for me. I close this acknowledgement confessing my faith.